Build Simul
https://doi.org/10.1007/s12273-024-1153-2

Impact of radiative cooling on the energy performance of courtyards in Mediterranean climate

Carlos-Antonio Domínguez-Torres[1] (✉), Antonio Domínguez-Delgado[2]

1. Escuela Técnica Superior de Arquitectura, Universidad de Sevilla, Av. de Reina Mercedes, 2; 41012 Sevilla, Spain
2. Department of Applied Mathematics 1, Escuela Técnica Superior de Arquitectura, Universidad de Sevilla, Av. de Reina Mercedes, 2; 41012 Sevilla, Spain

Research Article

Abstract

Radiative cooling has proven to be a useful tool to address the problems of lack of comfort and excessive energy consumption in situations of high temperatures, overheating and heat waves. Likewise, incorporating courtyards in warm climate zones has been found to be highly beneficial in addressing similar challenges. Hence, there is interest in analyzing the combined effects of both: radiative cooling and courtyards. This paper presents an analysis of the impact of the application of radiative cooling on a courtyard using a comprehensive simulation approach that includes a CFD model for the thermodynamic airflow in the adjacent roofs and inside the courtyard, equations for the transient heat conduction through roofs, walls and courtyard slabs, and a hybrid raytracing-radiosity model for the evaluation of the solar radiation reaching the building surfaces and its reflections, both of specular and diffuse origin, and for the calculation of the thermal radiation exchange, especially with the sky. The results show that in the hot season, the courtyard with radiative cooling always provides lower temperatures than the initial courtyard does, with a temperature range of 18.33 °C to 33.78 °C, compared to a range of 19.32 °C to 38.00 °C in the initial courtyard, and producing a greater difference with outdoor temperatures that can reach 12 °C versus 8 °C for the reference case. In addition, it was found that the courtyard with radiative cooling is able to significantly reduce the observed nighttime overheating by providing lower temperatures than the outdoor temperatures in the 50% of the nights studied. It was also found that the thermal loads to achieve indoor thermal comfort in the spaces adjacent to the courtyard were reduced by 63.46% to 69.85%.

Keywords

radiative cooling
passive cooling
CFD
three-dimensional modeling
energy saving
thermal comfort

Article History

Received: 30 March 2024
Revised: 14 May 2024
Accepted: 08 June 2024

1 Introduction

In recent decades, two major concerns have been taking shape worldwide: on the one hand, a burgeoning concern is emerging regarding global energy demand, propelled by the exponential surge in consumption; on the other hand, and directly linked to the above, the increase in the Earth's average temperature, known as global warming.

Both issues are closely linked, since an increase in energy consumption leads to an increase in greenhouse gases, the direct cause of global warming, which in turn leads to an increase in energy consumption in many areas of human activity, such as housing, where the expected rise in temperatures and increasingly frequent heat waves will lead to an increase in the energy consumed to achieve indoor thermal comfort (IPCC 2014).

In the Mediterranean zone, there is an expectation of a 3 or 4 °C increase in maximum summer temperatures by 2050 (Vautard et al. 2014), while, more specifically, in the urban environment, the urban heat island (UHI) effect can cause temperature increases that some projections put at up to 10 °C (Santamouris and Yun 2020).

Santamouris (2016) analyzed the impact of this temperature increase on buildings, concluding that there will be a significant rise in the demand for energy to cool buildings in the coming decades. While the global cooling

E-mail: cdtorres@us.es

consumption of the residential sector constituted almost 4.4% of the total heating and cooling demands of buildings in 2010, forecasts suggest it will escalate to 35% by 2050 and 61% by 2100 (Isaac and van Vuuren 2009).

Additionally, while the residential sector's heating energy demand is anticipated to remain steady or slightly decrease in the coming years, the overall heating and cooling consumption of buildings could surge by up to 67% by 2050 and 166% by 2100 compared to 2010 levels, exacerbating global energy and environmental challenges (Isaac and van Vuuren 2009).

Conversely, global warming is expected to have a heightened impact on disadvantaged populations, potentially leading to instances of internal thermal discomfort and energy poverty (Santamouris and Kolokotsa 2015).

According to European Commission (2015), the combined energy consumption of buildings in the public and private sectors amounts to nearly 40%. Therefore, taking into account the above-mentioned issues, it is imperative to reduce the environmental impact of the existing building stock. Hence, any initiative targeting the reduction of energy usage in buildings is of paramount importance. In this regard, many regulations have emerged, such as the EU directives outlined in H2030 European Commission (2014), which stipulate a goal of achieving a minimum 32.5% enhancement in energy efficiency by 2030.

A distinct goal in enhancing energy efficiency, particularly in the Mediterranean region, involves addressing the building stock constructed prior to the enactment of the initial regulatory standards governing energy demand in buildings NBE-CT-79 (1979). Most of these dwellings were built during the middle decades of the last century and constitute a substantial proportion of the current building stock. According to data from the National Statistics Institute (SNSI 2019), in Spain about a 56% of the existing housing stock was built in that period. Thus, the introduction of energy-saving measures on this social housing stock aids in furnishing interior comfort for low-income inhabitants and addressing energy poverty, leading to compliance with European energy targets and diminishing global warming through decreased energy usage.

In this scenario, employing methods that effectively harness environmental and climatic resources, coupled with the adoption of tailored designs suited to local climatic conditions, can greatly enhance the energy efficiency of buildings and, thus, reduce their energy consumption. It is widely recognized that traditional buildings employ passive strategies effectively to meet climatic demands, achieving optimal indoor comfort with minimal energy consumption. For instance, these strategies include the implementation of cooling techniques such as radiative cooling (Amraoui et al. 2021) or appropriate design such as courtyards (Bahadori 2011).

Summers in southern Spain, similar to most parts of the Mediterranean area, are hot, rainless, and with high levels of solar irradiation. As noted in Kuhn et al. (2001), in such climates, overheating concerns lead to increased energy usage for cooling buildings. Therefore, minimizing heat transfer into the building during the warmer months is crucial to reduce the energy needed to maintain indoor comfort and face the increasingly frequent heat waves predicted by climate change projections.

In this regard, in the warm season in the Mediterranean area, the skies are usually clear. Hence, it appears advisable to utilize radiative exchange with the sky via radiative cooling techniques as a method to mitigate the cooling load. On the other hand, as far as design is concerned, the incorporation of courtyards in dwellings is a tool for the creation of a comfort space in warm season, as well as influences on a better energy performance of the building (Zamani et al. 2018).

Research on radiative cooling techniques has been going on for several decades. In Hay and Yellott (1969), an early application of radiative cooling in buildings was introduced. This application used an integrated rooftop pond/massive roof and a movable insulation system. Since this pioneering study, numerous other investigations have focused on improving its development and analyzing the associated problems that limit the applicability of this technology in buildings.

In the wake of this pioneering study, there has been a great deal of research into the improvement of its development and the analysis of the associated problems which limit the applicability of this technology for use in buildings (Lu et al. 2016; Goldstein et al. 2017). In summary, traditional radiative cooling devices typically comprise complex multilayer structures and reflective metallic backplates, rendering them unsuitable for household applications (Das et al. 2023).

Considering on the one hand that the use of selective materials whose optical properties match the atmospheric window of 8 μm to 13 μm is the most significant factor affecting radiative cooling performance (Granqvist and Niklasson 2018) and on the other hand, the difficulties involved in the application of other radiative sky cooling techniques in buildings, as mentioned above, it is logical that the use of such selective materials for roofs and walls cladding is one of the most widely used radiative cooling techniques for building applications today, both in new buildings and in refurbishment.

In this regard, the intensive development of such selective materials over the last two decades should be highlighted. In this respect, two types of radiative cooling materials can

be distinguished: those that achieve nocturnal radiative cooling only and those that are also capable of producing diurnal radiative cooling. In Chen et al. (2020) an exhaustive review is made of these materials and the difficulties involved in their use: manufacture and applicability in buildings. Although no detailed information is given on the costs of these materials, it is mentioned that they are usually significantly more expensive than conventional materials used for building envelope cladding. In this work, it is said that materials like nanophotonic surfaces (Raman et al. 2014), and metamaterial surfaces (Zhai et al. 2017) are able to provide diurnal a nocturnal cooling. Thus, recent research indicates that advanced nanophotonic materials have demonstrated the capability to deliver efficient sub-ambient daytime radiative cooling (Rephaeli et al. 2013; Raman et al. 2014; Zhai et al. 2017) and in Fernandez et al. (2015) it was found cooling energy savings in the range of 45% and 68 % in a study conducted in the US.

Despite the interesting radiative properties of these types of materials, most single-layer polymer nanocomposites face challenges in practical application due to their high cost, fragility, and suboptimal cooling performances caused by low thermal emissivity, while other reflective materials, such as silver film, increase the cost and reflect light Das et al. (2023); Chen and Lu (2020).

In this regard, in the Mediterranean area the use of white paint, which provides high rates of solar reflectivity, is widespread. Commercial paints in this respect are capable of providing a solar reflectivity of up to 0.83 with a thermal reflectivity of 0.94 (INDEX 2024), while more traditional paints used in this geographical area provide solar reflectivities in a range of 0.70 to 0.8 and thermal reflectivities in a range of 0.70 to 0.85 (Domínguez-Delgado et al. 2020)

On the other hand, recent advances in high emissive paints have led to very useful paints for building applications. Thus, Das et al. (2023) introduced an ultra-white and ultra-emissive magnesium oxide (MgO)-polyvinylidene fluoride (PVDF) nanocomposite able to lower the temperature 7 °C underneath sub-ambient conditions, while exposed to direct sunlight, and exhibiting a solar reflectance of 96.3% and a thermal emissivity of 98.5% at the atmospheric transmission window, showcasing water-resistant hydrophobic characteristics. This paint can be effortlessly applied to pavers, wooden sticks, etc., with exceptional uniformity and strong adhesion, which makes it very suitable for application in buildings.

In addition to the widespread use of reflective paints in traditional architecture in the Mediterranean area, as well as in other areas with temperate and warm climates, it is possible to incorporate climate resilience strategies into current architectural practice (Chandel et al. 2016). An illustration of this concept can be seen with courtyards, whose inclusion in buildings stands out as one of the more efficient methods of reducing energy usage and tempering outdoor climatic conditions. By creating a microclimate within the building's central area, courtyards play a pivotal role in enhancing indoor thermal comfort and in diminishing the heat island effect at the urban level.

Although some studies focus on the effect of albedo on the energy performance of courtyards (Taleghani et al. 2014; Zamani et al. 2018), there is a gap in the literature on the impact on the energy performance of the courtyard of the application of radiative cooling techniques involving all surfaces around the courtyard, including roofs. Radiative cooling of the surfaces that make up the courtyard, walls and floor, can be expected to produce a decrease in the courtyard air temperature, while the reduction of the heat stored by the walls should reduce the heat flow into the interior. In addition, the use of radiative cooling coats on the roof, while reducing the heat flow towards the interior of the building through the roof, also produces a cooling of the air layer on the roof, which, due to the wind drag effect and its higher density, can cause a cold air fall effect inside the courtyard that can have a further cooling effect on the courtyard as a whole.

The analysis of the combination of the specific thermodynamics of the courtyards and the effect on it of the radiative cooling techniques applied to the adjacent roofs and walls constitutes a major challenge since the analysis of such effects involves the use of turbulent CFD models for the thermodynamic airflow over the roofs and adjacent courtyard, dynamic conduction modeling of heat transfer through the ground, walls and roofs, evaluation of radiative heat exchange of roof surfaces to the sky, of courtyard surfaces to the sky, and of courtyard surfaces to each other, plus evaluation of absorbed direct and diffuse solar radiation and reflections of these between courtyard surfaces.

A variety of software has been used to simulate the energy performance of courtyards, but most of them show limitations in correctly describing the energy performance of courtyards. This is the case of DesignBuilder which is a specific software for architecture which uses the software EnergyPlus as calculation engine. However, its use to predict the energy performance of courtyards is not adequate as shown in Al-Hafith et al. (2017) where a significant lack of accuracy was found to simulate the temperature of courtyards.

Similarly, courtyard research has recently been using different tools for urban microclimate simulation such as the ENVImet software (Tsoka et al. 2018). This software, despite its great predictive capacity for the determination of microclimates in urban areas, has characteristics that

do not allow it to provide accurate data in the case of courtyards. Thus, in López-Cabeza et al. (2018) the effectiveness of the ENVI-met software to predict the thermodynamic performance of courtyards is evaluated by comparing field data with data from software simulations performed with ENVI-met for three different courtyards in southern Spain. The study's findings revealed a notable variance between the observed and simulated air temperatures within the courtyards, and the authors concluded that the data produced by ENVI-met are not sufficiently precise to be utilized as input variables in the calculation of building's energy consumption and therefore cannot be used to accurately determine comfort levels in the courtyard itself.

Another tool developed in recent years is the Ladybug software, which integrates various simulation engines within the graphical interface of the Grasshopper plugin for Rhinoceros (Sadeghipour Roudsari and Pak 2013). Ladybug performs the building energy calculation using EnergyPlus software in combination with OpenFOAM CFD software for microclimate flows. Although the fact that it is open source and the ease of use through Grasshopper can make it interesting for the determination of urban microclimates in general, and courtyards in particular, its use has some limitations such as it has a single CFD model implemented through OPENFOAM, which makes it unable to adjust the CFD calculations well to each case and, in the particular case of courtyards, its results provide even larger tracking deviations than ENVImet, as shown in López-Cabeza et al. (2021) .

In light of this background, in order to adequately describe the energy behavior of the courtyard and the building when radiative cooling procedures are applied to the roofs and walls adjacent to the courtyard, the need to develop specific simulation models capable of accurately dealing with the various physical processes involved seems clear.

In this paper, the impact on the energy performance of a courtyard of the implementation of a radiative cooling technique consisting of the application of an ultra-emissive paint to the roof and walls of the courtyard in the context of a Mediterranean climate is analyzed.

For this purpose, a comprehensive numerical model is developed that is capable of describing with a high degree of accuracy the various physical processes involved, namely: the solar absorption of the roof, the thermal exchange of the roof with the sky, the convective thermal exchange with the airflow on the roof, the turbulent thermodynamics of the air on the roof and in the courtyard, the buoyancy effect of the air, the solar absorption of the courtyard surfaces of the diffuse and direct solar radiation, the exchange by reflection between these surfaces of both types of solar radiation, the thermal radiation exchange of the courtyard surfaces with the sky and with each other, and finally the heat conduction through the roof and wall surfaces with the interior of the building and through the ground.

The numerical code was developed using the open-source software *FreeFem++* (Hecht 2012), and subsequently was experimentally validated through a case study situated in Seville, Spain. Then, the model was used to assess the impact on the thermal performance of the courtyard of the application of a radiative cooling technique consisting of the application of ultra-emissive paint to the roofs and walls adjacent to the courtyard for a typical summer time period in the city of Seville (Spain).

In line with the above, it can be said that the innovative contributions of this work are: first, the analysis of the effects of the application of an easy-to-use radiative cooling technique consisting of the use of an innovative ultra-emissive paint on the thermal behavior of a courtyard and on the associated loads to obtain comfort in adjacent spaces, and this for a building with poor thermal insulation characteristics, which is a typical representative of about 50% of the building stock in Spain; also involving the effect of radiative cooling of roofs on the thermal behavior of the courtyard, topic not covered in the previous literature. Second, the development of a numerical simulation model combining CFD turbulent modeling, thermal conduction, and a hybrid raytracing-radiosity model to evaluate long-wave radiative exchanges with the sky and between the surfaces of the courtyard itself, as well as short-wave reflections, a model that has demonstrated its ability to accurately simulate the thermal performance of the courtyard.

The paper is organized as follows: in Section 2 the research methodology is described; in Section 3 the case study is presented; Section 4 develops the energy modelling underlying the simulation model; Section 5 describes the numerical approach; in Section 6 the results of the validation procedure of the simulation model are shown; Section 7 analyzes the impact of the implemented ultra-emissive paint on the thermal and energy performance of the courtyard and compares it to the base case; finally, in Section 8 conclusions are drawn. Furthermore, appendices A, B, and C offer supplementary content so as not to overload the exposition of the article.

2 Methodology

As stated in Forouzandeh (2022), the assessment of the energy performance of buildings in urban areas is a task that can be approached in a variety of ways: by means of an experimental approach based on measurements taken in the building in question, through an approximation based on the use of numerical models, and finally a combined strategy that includes measurements and simulation.

By conducting field measurements, it is possible to capture the intricate nature of buildings energy performance. Its main disadvantage lies in experimental uncertainties and high costs (Blocken 2015). At the same time, the results obtained are exclusively applicable to the case study and the climatic conditions under which the measurements were carried out, and it is not reliable to extend the conclusions obtained to circumstances other than those under which the experimental measurements were taken.

For its part, the methodology of building energy analysis based on the use of numerical simulation models has the advantage of being fully controllable, allowing the energy performance of a building to be modeled taking into account multiple variables such as geometry, construction materials, local climate and the intended use of the building, it lacks experimental uncertainties and its cost is low compared to experimental data collection; but for a simulation model to be used with confidence, it must be rigorously validated (Judkoff et al. 2008).

This study is starting in its first stage with the development of a numerical simulation model to predict the energy performance of a courtyard subjected to different environmental and design conditions in the framework of the implementation of radiative cooling techniques based on the application of cool and highly emissive coats on the courtyard envelope and in the adjacent roofs, as described in Section 4. In the same initial phase, the monitoring equipment was prepared to carry out the data collection in the case study, as detailed in Section 6.1.

In the second stage, data were collected by monitoring during a period of high temperatures typical of the summer in southern Spain, while at the same time simulation data acquisition was performed for the same time period using the numerical model previously developed in the first stage. These experimental data acquisition and simulation processes are described in Sections 5 and 6.2.

Next, in the third stage, a validation procedure was performed to ensure the accuracy of the results of the simulation model presented using a set of statistical indices common in the validation of building energy software and a qualitative comparative analysis, as described in Section 6.

In the following stage, the numerical model is used to compute the impact on the energy performance of the courtyard of implementing a radiative cooling technique based on the use of highly emissive coats by performing a comparative analysis of the energy performance for both cases, as described in Section 7.

Figure 1 provides an overview of the methodology employed.

3 Case study

3.1 Test building

The chosen building for conducting experimental measurements is situated within the city of Seville, Spain, (latitude 37°22′, longitude −5°58′, altitude 14 m), in a centric area of the city, Figure 2.

The selected building can be considered as a representative case of the social housing built in southern Spain before the enactment of the first Spanish legislation for the regulation of energy demand in buildings NBE-CT-79 (1979). The building is located within El Plantinar, a social housing development erected during the 1960s, Figure 3. The construction style of this development reflects the prevalent construction style of social housing during that period, characterized by a notable absence of energy insulation measures.

The courtyard case-study has an irregular geometry, Figure 4(a), and is surrounded by five-story buildings on the north-east side, whilst on the south-west side the building has nine stories. Figure 4(b) shows a floor plan with the dimensions of the courtyard.

This irregular configuration of the courtyard and surrounding buildings represents a highly demanding test to validate the accuracy of the simulation model and provides additional strength to the validation process. In Figure 5 the appearance of the courtyard under study is depicted.

All the walls surrounding the courtyard are painted white, so according to (Fernández Díaz 2010) and initial solar reflectivity of 0.65 and a thermal emissivity of 0.85 are assumed. The layout of the walls is depicted in Figure 6,

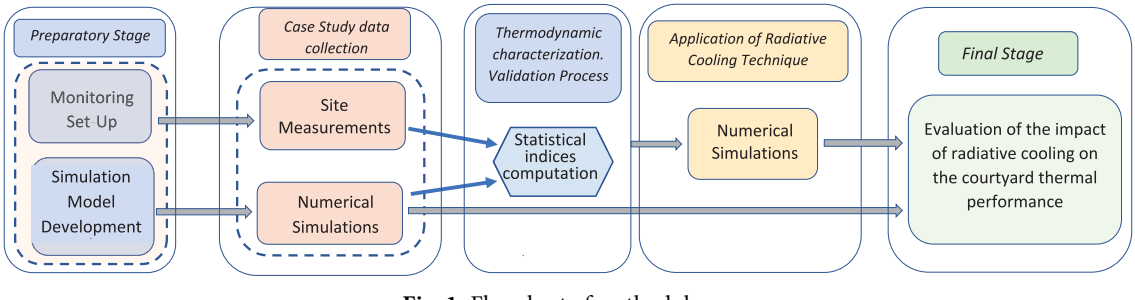

Fig. 1 Flowchart of methodology

Fig. 2 Urban location (building case study marked in red)

Fig. 3 El Plantinar development aerial view (building case study marked in red)

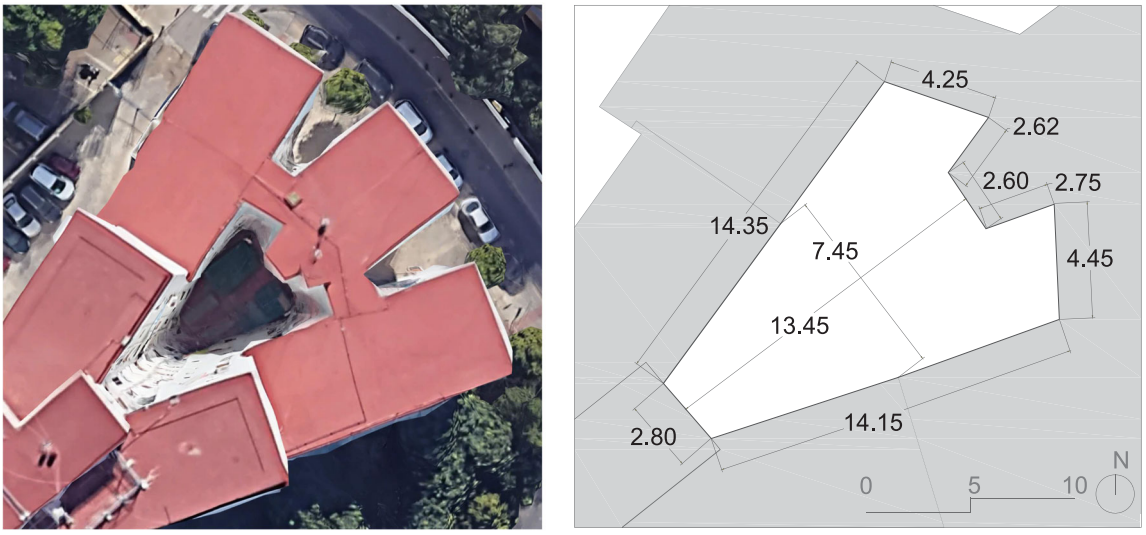

(a) (b)

Fig. 4 (a) Courtyard aerial view; (b) courtyard plan with dimensions in meters

(a) (b)

Fig. 5 (a) North-east courtyard view; (b) south-west courtyard view

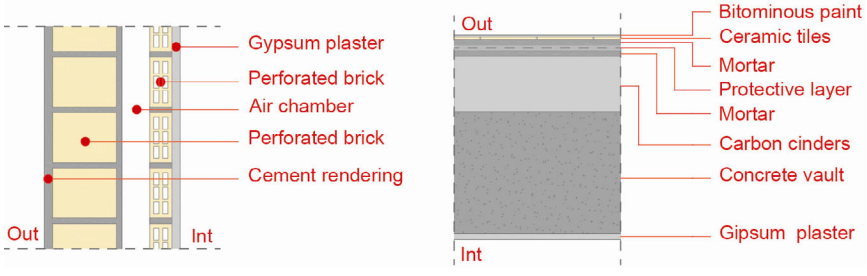

Fig. 6 Layout of: (left) courtyard walls; (right) surrounding roofs

whilst the thermophysical values and dimensions of the wall layers are described in Table A1 in Appendix A.

As depicted in Figure 4(a), the roofs are flat and feature a coating of bituminous paint on their outer surface. Hence, a solar radiation absorptivity coefficient of 0.8 has been chosen for the outer roof surfaces, in line with typical values reported for this type of coating (Fernández Díaz 2010). Figure 6 shows the layout of the roofs, while in Table A2, in Appendix A, the thermophysical values and dimensions of the roofs layer are described. This appendix also shows the thermophysical characteristics of the courtyard floor slab in Table A3.

This courtyard configuration is considered the reference or base case.

3.2 Climate conditions

Figure 7 displays the climatic chart for Seville, presenting values sourced from the Spanish Governmental Climate Database (AEMET 2010). According to the referenced data, the average temperature for the year is 19.2 °C, with maximum averages of 40 °C occurring in July and August, and a minimum average of 5.7 °C noted in January. In accordance with the Köppen-Geiger climate classification system, the region's climate falls under the category of Mediterranean Csa.

Temperature measurements were taken from July 1 to July 8, 2023, so in the heart of the hot season. For this week, outdoor temperatures ranged from a minimum of 19.09 °C to a maximum of 41.84 °C, with a maximum of the global solar radiation of 827 [W/m^2]. The chosen time period presents the typical characteristics of summer in southern Spain with high values of ambient temperature and solar radiation and with little or no cloud cover, being therefore a weather framework that can be considered as very suitable for the use of radiative cooling techniques.

The time span considered for validation can be assumed adequate based on previous studies incorporating building energy software and outdoor CFD modeling (Forouzandeh 2018; Antoniou et al. 2019). Taking into account the need to capture the inertial effects on the courtyard temperatures caused by the thermal masses of the surrounding envelope,

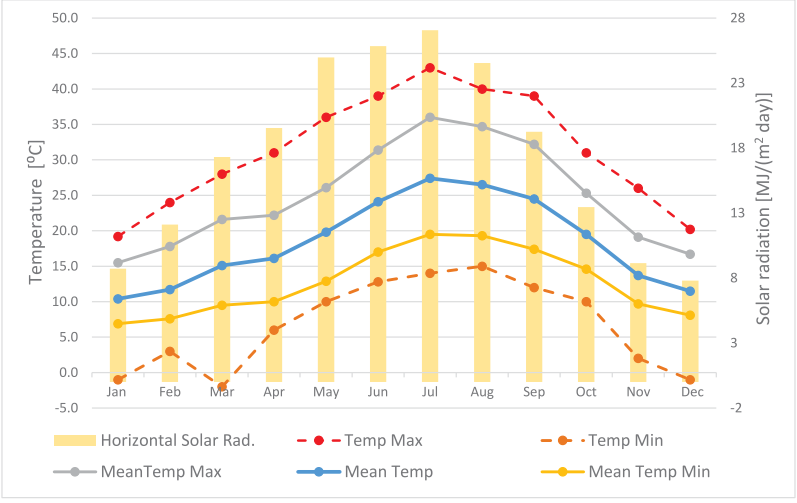

Fig. 7 Climatic chart of Seville

the days from July 1 to July 3 were used only as warming period for the numerical model.

4 Energy modelling

In this section, the physical basis and mathematical associated formulations utilized in the simulation model are shown. These formulations are based on building physics literature and contemporary scientific research on heat transfer EnergyPlus (2021); Bejan (1992); Mills (1998); Cengel (1992).

Experimental results are usually only applicable to situations similar to those encountered in the process of such experimental data collection. Therefore, to estimate or evaluate other different situations, weather climatic, geometric or material, it is necessary to use numerical simulation models that, once validated, allow accurate and reliable results to be obtained. The first step in developing a numerical simulation model is to establish the physical foundations on which it will be based, and those in the present case are described next.

4.1 Physical fundamentals of the energy performance and radiative cooling

Herein, a general overview of the physical fundamentals and underlying assumptions is provided. The energy behavior of the courtyard and adjacent zones is driven by:

- Heat gain on the outer surfaces of the roof and courtyard walls as a result of incident solar irradiation.
- Exchange of solar radiation due to reflections among the surfaces of the courtyard.
- Thermal radiative exchange between the outer surfaces of the roof and courtyard walls and the sky.
- Thermal radiative exchange between the outer surfaces of the courtyard. Heat exchange by convection between the outer surfaces of the roof and the courtyard and the outdoor air.
- Heat transfer by conduction through the roof, courtyard walls, and floor slab.
- Turbulent thermal flow combined with natural covection for outdoor air. Convective and radiative heat exchange between surfaces and air inside the building spaces adjacent to the courtyard

For interior spaces adjacent to the courtyard, the air is assumed to have a uniform temperature and is therefore assigned a single value. This simplification is widely accepted in building simulation models like EnergyPlus (EnergyPlus 2021), and is a common feature in academic literature (Cattarin et al. 2018; Domínguez-Torres et al. 2022).

4.2 Solar radiative model

The solar radiation model distinguishes between the roof and wall surfaces, being the specific model for each type of surface described in the next sections.

4.2.1 Solar radiative model for the roof

The absorbed solar radiative flux on the external surfaces of a roof is computed as

$$q^{\mathrm{SW}} = \alpha^{\mathrm{SW}} \cdot \left(I_{\mathrm{b}} \cdot \cos(\theta) + I_{\mathrm{d}} \cdot F_{\mathrm{r,s}} + I_{\mathrm{g}} \cdot F_{\mathrm{r,g}} + I_{\mathrm{surr}} \cdot F_{\mathrm{r,surr}} \right) \quad [\mathrm{W/m^2}] \tag{1}$$

where α^{SW} stands for the solar absorptance of the external roof surface, θ signifies the angle of incidence of the sun's rays on the roof, I_{b} represents the intensity of the beam solar radiation, I_{d} stands for the intensity of the diffuse radiation that is reflected by the sky onto the roof, $F_{\mathrm{r,s}}$ is the view factor between the roof and the sky, I_{g} signifies the

intensity of the solar radiation reflected by the ground onto the roof, and $F_{r,g}$ stands for the view factor between the roof and the ground. Lastly, I_{surr} denotes the intensity of the radiation reflected by the surrounding buildings, while $F_{r,surr}$ represents the view factor between the roof and these buildings.

In the analyzed case study, it is assumed that the roof is flat, therefore $F_{r,g} = 0$.

4.2.2 Solar radiative model for the courtyard surfaces

The methodology used for the calculation of solar radiation absorbed by the courtyard surfaces follows the methodology introduced in Domínguez-Torres et al. (2019). An overview of this methodology is presented below and can be found in more detail in the aforementioned work.

For the surfaces that make up the courtyard, walls and floor, the solar radiative model must take into account, in addition to the direct and diffuse solar radiation from the sun and the sky that reaches all these surfaces, the exchanges between these surfaces due to reflections of specular and diffuse solar radiation.

To calculate the solar radiation absorbed by these surfaces, a triangular mesh $\mathcal{T}_{C,h}$ of the surfaces surrounding the courtyard is considered.

Firstly, every triangle $T_i \in \mathcal{T}_{C,h}$ impacted by direct solar radiation is identified. In this regard, the unitary solar position vector $\vec{S}(t)$, indicating the direction from the building's location to the sun at time t, is utilized. Next, an examination is conducted for each triangle $T_i \in \mathcal{T}_{C,h}$ to ascertain whether the line originating from the barycenter of T_i with the directional vector $\vec{S}(t)$ intersects with surfaces within the courtyard or external obstacles. When an intersection takes place, the direct solar radiation reaching the triangle is null. Otherwise, the product $\vec{S}(t)\cdot\vec{n}_i$ is evaluated, being $\vec{n}_i$ the unitary exterior vector to T_i. If the resulting value is negative, it indicates that the solar position is deemed opposite to the triangle, and thus, the incident direct radiation on T_i is set to zero. In case of a positive result, the incident direct radiation on T_i is determined by $I_i^b(t) = I^b(t)\cos(\theta_i(t))$, where $\theta_i(t)$ represents the angle of incidence of the direct beam radiation onto T_i. Next, vector analysis is applied to achieve (Sproul 2007):

$$I_i^b(t) = I^b(t)\vec{n}_i \cdot \vec{S}(t) \tag{2}$$

Then, the series of specular radiation originating from T_i is computed. This sequence concludes once the specular reflective ray either exits towards the sky or its intensity diminishes below a preset threshold. Then, we note by γ_i the set of triangles consisting of T_i and those reached by some of the specular reflections originating from T_i.

For each $T_j \in \gamma_i$, $\vec{r}_{i,j}^{\,b,inc}(t)$ represents the incident unit vector on T_j originating from a specular reflection at T_i, while $\vec{r}_{i,j}^{\,b,spe}(t)$ denotes the reflective specular unit vector leaving T_j originated by $\vec{r}_{i,j}^{\,b,inc}(t)$.

The intensity of the incident ray with direction $\vec{r}_{i,j}^{\,b,inc}(t)$ is labeled as $I_{i,j}^{b,inc}(t)$, while the intensity of the specular reflective ray departing T_j in the direction of $\vec{r}_{i,j}^{\,b,spe}(t)$ is denoted as $I_{i,j}^{b,spe}(t)$. Next, the component of the specular radiative ray incident on T_j, which is perpendicular to the surface, is computed as:

$$I_{i,j}^{b,n}(t) = I_{i,j}^{b,inc}(t)\,\vec{n}_j \cdot \left(-\vec{r}_{i,j}^{\,b,inc}(t)\right)$$

Finally $I_j^s(t)$ is the variable that aggregates the radiation of specular origin conveyed by the rays arriving at T_j at time t. For T_i, $\vec{r}_{i,i}^{\,b,inc}(t) = -\vec{S}(t)$, $I_{i,i}^{b,inc}(t) = I^b(t)$ and $I_{i,i}^{b,n}(t) = I_i^b(t)$.

Then, for any $T_j \in \gamma_i$, the computational sequence of the proposed three-dimensional ray tracing algorithm unfolds as:

Step 1: The first step involves computing the specular reflection vector from T_j:

$$\vec{r}_{i,j}^{\,b,spe}(t) = \vec{r}_{i,j}^{\,b,inc}(t)\mathbf{R}_j \tag{3}$$

where $\mathbf{R}_j$ is the Householder transformation matrix for triangle T_j:

$$\mathbf{R}_j = I - 2\vec{n}_j \otimes \vec{n}_j \tag{4}$$

The vector $\vec{r}_{i,j}^{\,b,spe}(t)$ is normalized to ensure the handling of only unitary directional vectors.

Step 2: The possible intersection of the specular reflection from T_j with some triangle $T_k \in \mathcal{T}_{C,h}$ is determined. To accomplish this, a straight line originating from the barycenter B_j of T_j with direction $\vec{r}_{i,j}^{\,b,spe}(t)$ is constructed. If this line doesn't hit any triangle belonging to $\mathcal{T}_{C,h}$ this means that the specular reflection leaves to sky and the sequence of reflections with origin in T_i finishes. Case contrary, the triangle $T_k \in \mathcal{T}_{C,h}$ where the specular reflection from T_j given by the described straight hits is identified and the following steps are done.

Step 3: $I_{i,j}^{b,spe}(t)$ is calculated by:

$$I_{i,j}^{b,spe}(t) = \rho_j^s I_{i,j}^{b,n}(t)$$

where ρ_j^s is the specular reflectivity of triangle T_j.

Step 4: Then, the intensity of the normal incident specular radiation $I_{i,k}^{b,n}(t)$ on T_k is computed by

$$I_{i,k}^{b,n}(t) = I_{i,k}^{b,inc}(t)\,\vec{n}_k \cdot \left(-\vec{r}_{i,k}^{\,b,inc}(t)\right)$$

where $I_{i,k}^{\mathrm{b,inc}}(t) = I_{i,k}^{\mathrm{b,spe}}(t)$ and $\vec{r}_{i,k}^{\,\mathrm{b,inc}}(t) = \vec{r}_{i,k}^{\,\mathrm{b,spe}}(t)$. The value of $I_{i,k}^{\mathrm{b,n}}(t)$ is then accumulated on $I_k^{\mathrm{s}}(t)$. Then, if $I_{i,k}^{\mathrm{b,spe}}(t)$ falls below the predetermined threshold for residual specular radiation, the computation is regarded as complete. If not, the process iterates steps 1, 2, 3 and 4 again for T_k.

Finally, for every triangle $T_i \in \mathcal{T}_{\mathrm{C,h}}$ the total radiation of specular origin reflected from the other triangles that reaches T_i is stored in the variable $I_i^{\mathrm{s}}(t)$.

To compute the diffuse solar radiation absorbed by every triangle $T_i \in \mathcal{T}_{\mathrm{C,h}}$ it should be noted that the radiation incident on T_i comprises the initial radiation reaching T_i, namely $I_i^{\mathrm{b}}(t)$, $I_i^{\mathrm{d}}(t)$, $I_i^{\mathrm{r}}(t)$, in addition to radiation from specular reflections $I_i^{\mathrm{s}}(t)$, along with reflected diffuse radiation from the triangles of solid cell faces. Therefore, the radiation diffusely reflected from triangle T_i at time t is:

$$E_i^{\mathrm{SW}}(t) = \rho_i^{\mathrm{d}}\left[A_i\left(I_i^{\mathrm{b}}(t) + I_i^{\mathrm{d}}(t) + I_i^{\mathrm{r}}(t) + I_i^{\mathrm{s}}(t)\right) + \sum_{j=1}^{N} E_j^{\mathrm{SW}}(t) F_{j,i}\right] \tag{5}$$

where ρ_i^{d} is the diffuse reflectivity of T_i, A_i is the area of T_i and $E_i^{\mathrm{SW}}(t)$, $E_j^{\mathrm{SW}}(t)$ denote the aggregate shortwave radiation reflected from the triangles T_i, T_j and $F_{j,i}$ is the view factor between T_j and T_i with origin in T_j.

Given that $E_j^{\mathrm{SW}}(t) = A_j J_j^{\mathrm{SW}}(t)$ where $J_j^{\mathrm{SW}}(t)$ and A_j are the radiosity and the area of T_j respectively, and taking into consideration that $F_{j,i}\, A_j = F_{i,j}\, A_i$, the radiosity $J_i^{\mathrm{SW}}(t)$ is obtained from Equation (6) as:

$$J_i^{\mathrm{SW}}(t) = \rho_i^{\mathrm{d}}\left[I_i^{\mathrm{b}}(t) + I_i^{\mathrm{d}}(t) + I_i^{\mathrm{r}}(t) + I_i^{\mathrm{s}}(t) + \sum_{j=1}^{N} J_j^{\mathrm{SW}}(t) F_{i,j}\right] \tag{6}$$

Applying Equation (6) to each $T_i \in \mathcal{T}_{\mathrm{C,h}}$, it is obtained the radiosity system of equations:

$$\mathbf{A}^{\mathrm{SW}} \cdot \mathbf{J}^{\mathrm{SW}}(t) = \mathbf{E}^{SW}(t) \tag{7}$$

with

$$\mathbf{A}^{\mathrm{SW}} = \begin{bmatrix} 1-\rho_1^{\mathrm{d}}F_{1,1} & -\rho_1^{\mathrm{d}}F_{1,2} & \cdots & -\rho_1^{\mathrm{d}}F_{1,N} \\ -\rho_2^{\mathrm{d}}F_{2,1} & 1-\rho_2^{\mathrm{d}}F_{2,2} & \cdots & -\rho_2^{\mathrm{d}}F_{2,N} \\ \cdots & \cdots & \cdots & \cdots \\ -\rho_N^{\mathrm{d}}F_{N,1} & -\rho_N^{\mathrm{d}}F_{N,2} & \ldots & 1-\rho_N^{\mathrm{d}}F_{N,N} \end{bmatrix}$$

$$\mathbf{J}^{\mathrm{SW}} = \begin{bmatrix} J_1^{\mathrm{SW}}(t) \\ J_2^{\mathrm{SW}}(t) \\ \cdots \\ J_N^{\mathrm{SW}}(t) \end{bmatrix}, \quad \mathbf{E}^{\mathrm{SW}} = \begin{bmatrix} \rho_1^{\mathrm{d}}(I_1^{\mathrm{b}}(t) + I_1^{\mathrm{d}}(t) + I_1^{\mathrm{r}} + I_1^{\mathrm{s}}(t)) \\ \rho_2^{\mathrm{d}}(I_2^{\mathrm{b}}(t) + I_2^{\mathrm{d}}(t) + I_2^{\mathrm{r}}(t) + I_2^{\mathrm{s}}(t)) \\ \cdots \\ \rho_N^{\mathrm{d}}(I_N^{\mathrm{b}}(t) + I_N^{\mathrm{d}}(t) + I_N^{\mathrm{r}}(t) + I_N^{\mathrm{s}}(t)) \end{bmatrix}$$

Then, the aggregate solar-origin radiation absorbed by $T_i \in \mathcal{T}_{\mathrm{C,h}}$ is calculated as

$$Q_i^{\mathrm{SW}}(t) = \alpha_i^{\mathrm{SW}} A_i \left[I_i^{\mathrm{b}}(t) + I_i^{\mathrm{d}}(t) + I_i^{\mathrm{r}}(t) + I_i^{\mathrm{s}}(t) + \sum_{j=1}^{N} J_j^{\mathrm{SW}}(t) F_{i,j}\right] \tag{8}$$

Hence, the intensity of radiation from solar sources absorbed by each triangle $T_i \in \mathcal{T}_{\mathrm{C,h}}$ is computed as

$$I_i^{\mathrm{SW}}(t) = \alpha_i^{\mathrm{SW}}\left[I_i^{\mathrm{b}}(t) + I_i^{\mathrm{d}}(t) + I_i^{\mathrm{r}}(t) + I_i^{\mathrm{s}}(t) + \sum_{j=1}^{N} J_j^{\mathrm{SW}}(t) F_{i,j}\right] \quad [\mathrm{W/m^2}] \tag{9}$$

4.3 Long-wave radiative flux

For the exterior roof surface the balance of long-wave radiation is estimated by

$$q^{\mathrm{LW}} = Q_{\mathrm{sky}}^{\mathrm{LW}} - Q_{\mathrm{roof}}^{\mathrm{LW}}$$

being $Q_{\mathrm{roof}}^{\mathrm{LW}}$ the intensity of the long-wave thermal radiation released by the external roof surface and $Q_{\mathrm{sky}}^{\mathrm{LW}}$ the long-wave radiation from sky.

To compute $Q_{\mathrm{roof}}^{\mathrm{LW}}$ the Stefan-Boltzmann law is used:

$$Q_{\mathrm{roof}}^{\mathrm{LW}} = \varepsilon\sigma T^4 \tag{10}$$

Here, ε represents the surface emissivity, T signifies the temperature in Kelvin degrees of the surface, and $\sigma = 5.67 \times 10^{-8}$ [W/(m²·K⁴)] is the Stefan-Boltzmann constant.

The sky's downwelling long-wave radiation $Q_{\mathrm{sky}}^{\mathrm{LW}}$ is influenced by various factors, with outdoor temperature, environmental relative humidity, and cloud cover being the most prominent. In essence, clouds absorb outgoing infrared (IR) radiation and emit thermal IR radiation at temperatures higher than those emitted by a clear sky. $Q_{\mathrm{sky}}^{\mathrm{LW}}$ can be computed as

$$Q_{\mathrm{sky}}^{\mathrm{LW}} = \varepsilon_{\mathrm{sky}}\sigma T_{\mathrm{a}}^4 \tag{11}$$

where $\varepsilon_{\mathrm{sky}}$ is the sky emissivity. Walton (1983) and Clark and Allen (1978) estimated that $\varepsilon_{\mathrm{sky}}$ can be approximated by

$$\varepsilon_{\mathrm{sky}} = \left(0.787 + 0.764\ln(T_{\mathrm{dp}}/273)\right)\cdot \left(1 + \frac{224}{10^4}n - \frac{35}{10^4}n^2 + \frac{28}{10^5}n^3\right) \tag{12}$$

where T_{dp} is the absolute dew point temperature and n is the opaque sky cover in tenths. This correlation for $\varepsilon_{\mathrm{sky}}$ is the used in this work.

To compute the long-wave radiation balance on every triangle $T_i \in \mathcal{T}_{\mathrm{C,h}}$, that is, on every triangle belonging to the surfaces of the courtyard, a radiosity system as the shown in Equation (7) is solved. Now, the matrix of the system is a

matrix $\mathbf{A}^{\mathrm{LW}}$ with the same structure as the matrix $\mathbf{A}^{\mathrm{SW}}$ but using the values ρ_i^{LW} of thermal reflectivity of every triangle T_i, instead of the solar diffuse reflectivity ρ_i^{d}. In this system, the unknowns are the long-wave radiosities $J_i^{\mathrm{LW}}(t)$ for every $T_i \in \mathcal{T}_{\mathrm{C,h}}$ and the terms of the RHS in the system are

$$E_i^{\mathrm{LW}} = \rho_i^{\mathrm{LW}} I_i^{\mathrm{sky}}(t) + \varepsilon_i^{\mathrm{LW}} \sigma T_i^4(t)$$

where $\varepsilon_i^{\mathrm{LW}}$ is the thermal emissivity of T_i and the intensity $I_i^{\mathrm{sky}}(t)$ of the sky downwelling long-wave radiation reaching T_i is computed as

$$I_i^{\mathrm{sky}}(t) = F_{\mathrm{sky},i} Q_{\mathrm{sky}}^{\mathrm{LW}}(t)$$

where $F_{\mathrm{sky},i}$ is the view factor between T_i and the sky. Finally, the net balance of thermal radiation on the triangle T_i at time t is given by:

$$I_i^{\mathrm{LW}}(t) = \varepsilon_i^{\mathrm{LW}} \left[I_i^{\mathrm{sky}}(t) + \sum_{j=1}^{N} J_j^{\mathrm{LW}}(t) F_{i,j} \right], \quad [\mathrm{W/m^2}] \tag{13}$$

4.4 View factor computation

The computation of the view factor between each par the triangles T_i and T_j belonging to $\mathcal{T}_{\mathrm{C,h}}$ is done using the methodology introduced in Domínguez-Torres et al. (2019), that is also used to calculate the view factor between every $T_i \in \mathcal{T}_{\mathrm{C,h}}$ and the sky.

4.5 Governing fluid equations

The governing equations for airflow and transport temperature involve the thermodynamic Navier-Stokes equations, incorporating a Boussinesq approximation for buoyancy effects. Furthermore, turbulence modeling is implemented using the RNG κ-ε model, as recommended by Coussirat et al. (2008), due to its improved performance in heat transfer calculations under low velocity air conditions.

Non-slip velocity conditions are imposed on solid surfaces throughout the computational domain. At the air inlet, the velocity and temperature values are derived from weather data. Slip conditions are applied at the top boundary, and free outflow conditions are implemented.

For temperature, the boundary values at the surfaces are the temperatures on the adjacent roofs, and the walls and floor of the courtyard. Initial conditions are set using the environmental values of the corresponding variables.

4.6 Thermal conduction through the roofs and the courtyard walls and floor

Heat conduction through the roofs and the courtyard walls is modeled by the following equation:

$$\frac{\partial T}{\partial t} - \nabla \cdot (\alpha \nabla T) = 0 \tag{14}$$

where the diffusivity coefficient α varies depending on the material composition of the walls, roofs, and floor slab layers.

Equation (14) must be closed with suitable boundary equations. Concerning the outer surfaces of the walls, roofs and floor slab, the boundary conditions are the energy balance equations for each surface S given by

$$\kappa_{\mathrm{S}} \frac{\partial T_{\mathrm{S}}}{\partial \vec{n}_{\mathrm{S}}} + q_{\mathrm{c,S}} + q_{\mathrm{S}}^{\mathrm{SW}} + q_{\mathrm{S}}^{\mathrm{LW}} = 0 \tag{15}$$

where $\vec{n}_{\mathrm{S}}$ denotes the outward normal vector to surface S, κ_{S} represents the conductivity of the material constituting the surface, and T_{S} stands for the surface temperature. Additionally, $q_{\mathrm{c,S}}$ signifies the intensity of the convective heat flux between the surface and the airflow that, following Zhai and Chen (2004), is computed directly as

$$q_{\mathrm{c,S}} = k_{\mathrm{air}} \left(T_{\mathrm{air}}(x_\delta) - T_{\mathrm{S}} \right)$$

being k_{air} the air conductivity, T_S the surface temperature and $T_{\mathrm{air}}(x_\delta)$ the air temperature at a point inside the thermal turbulent boundary layer of the flow. The calculation of $q_{\mathrm{c,S}}$ is explained in Section 5.3. Lastly, $q_{\mathrm{S}}^{\mathrm{SW}}$ and $q_{\mathrm{S}}^{\mathrm{LW}}$ represent the intensity of radiative flux of solar origin and the intensity of the balance of long-wave radiation on surface S. The computation methods for these quantities are detailed in Sections 4.2 and 4.3.

For the inner surfaces of the walls and roofs, the boundary conditions are described in Section 4.7, whilst for the boundary condition of the floor slab that is in contact with the soil the boundary condition is the temperature of soil taken from the EnergyPlus Weather (epw) file for Seville.

4.7 Indoor zones modeling

The temperatures of the courtyard walls and the adjacent roofs are influenced by the indoor temperatures T_z of the adjacent interior zones via Equation (14). So the values of T_z must be taken into account and incorporated into the overall energy model, their values being determined either by monitoring or by numerical simulation.

Two cases are considered for the indoor air temperature T_z: either T_z is in a free-running regime or on the contrary it is fixed at some predetermined value such as the comfort temperature.

In the case of assuming a fixed temperature for T_z it is

only necessary to use as boundary condition in Equation (14) the energy balance in the inner wall given by

$$\kappa \frac{\partial T_S}{\partial \vec{n}} + h_{c,r}(T_z - T_S) = 0 \tag{16}$$

where κ is the thermal conductivity of S, T_S is the temperature of the interior surface of the wall or roof, $\vec{n}$ is the unitary normal vector to the wall pointing to the interior of the zone and $h_{c,r}$ is the interior combined convective-radiative heat transfer coefficient whose value is taken as $h_{c,r}$ = 8.29 [W/(m^2·K)], as recommended in ASHRAE (1997).

This value of $h_{c,r}$ is commonly used into calculations for heat transfer within the interiors of buildings (Sanjuan et al. 2011).

If free evolution is considered, the indoor air temperature T_z must be calculated at each time t. The approximation considered here is:

$$\frac{dT_z(t)}{dt} = \frac{1}{C_z}\Big[\sum_j h_{c,r} A_j (T_j(t) - T_z(t)) + \dot{m}_{vent} c_{air} (T_v(t) - T_z(t)) + \dot{m}_{inf} c_{air} (T_i(t) - T_z(t) + \dot{m}_{sup} c_{air} (T_{sup}(t) - T_z(t))\Big] \tag{17}$$

where $h_{c,r}$ is the mixed convective-radiative heat transfer coefficient, A_j and $T_j(t)$ are the area and the temperature at time t of each surface j of the indoor zone; $\dot{m}_{vent}$, $\dot{m}_{inf}$ and $\dot{m}_{sup}$ represent the air flux in [kg/s] attributed to ventilation, infiltration, and systems delivering air at a temperature T_{sup}; c_{air} is the specific heat of the air and C_z is the heat capacity of the air zone; and $T_i(t)$ and $T_v(t)$ are the temperatures at time t of the infiltration and ventilation air which can be taken as the outdoor air temperature or the courtyard air temperature depending on the building design.

5 Numerical approximation

Herein, we present the numerical approximation employed to analyze the overall energy behavior of the courtyard derived from the modeling frameworks introduced in previous sections.

5.1 Numerical approximation overview

The numerical approximation is based on a tetrahedral 3D finite element discretization of the roofs and walls adjacent to the courtyard, and the floor slab of the courtyard. As a result of this 3D meshing, all exterior surfaces belonging to the roof, and the walls and floor of the courtyard are meshed by triangles which are used to perform the radiative calculations as described in the Sections 4.2 and 4.3. Likewise, the entire air region, inside the courtyard and on the roof

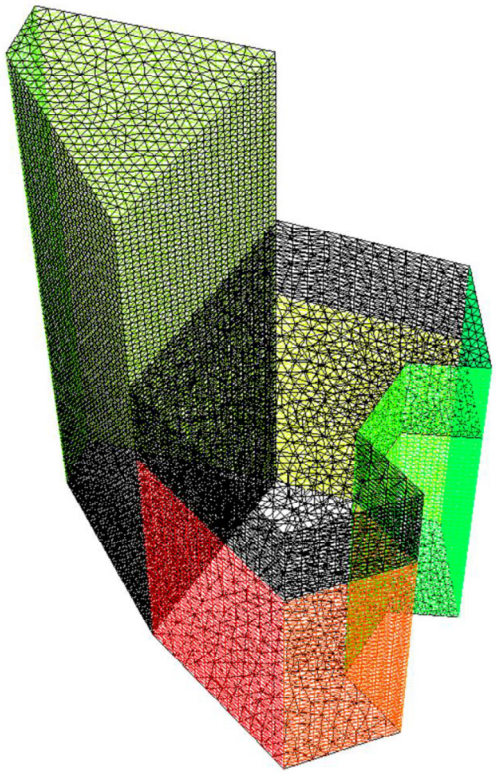

Fig. 8 Tetrahedral mesh of the air inside the courtyard

is also discretized by tetrahedra. In Figure 8 a view of the tetrahedral mesh of the air inside the courtyard is shown.

The complete calculation process was carried out by developing a computational code based on the previously presented model and utilizing the open-source *FreeFem++* software (Hecht 2012).

The computational code can be summarized in the following manner.

- Stage I – Preprocess:

I.A Geometry and material data entry: This phase involves entering and storing the geometry of the case study and the simulated environment. Additionally, the material data necessary for the simulations are entered and saved.

I.B Meteorological data input: Wind speed and direction, ambient air temperature, ambient relative humidity, solar radiation, and long-wave radiation incident on various surfaces are stored during this phase. These values can be sourced from standard weather files like the EnergyPlus Weather files, local meteorological stations, or derived from a model.

I.C Calculation and storage of view factors for the courtyard surfaces are performed.

I.D Computation of the matrix of the radiosity system for diffuse solar radiation and thermal long-wave exchanges. The computations of [I.C] and [I.D] are performed once and can be used as input data in the numerical code.

- Stage II – Time iterations:

II.A Initialization for $t = t_0$.

II.B At each time instance t_m, the following calculations are carried out:

- Updating of climatic variables.
- Updating of sky temperature.
- Calculation of solar radiation incident on courtyard surfaces and roofs.
- Computation of short-wave and long-wave radiative exchanges between courtyard surfaces.
- Computation of long wave radiative exchange of roofs and courtyard surfaces with sky.
- Upgrading of border conditions.
- Numerical resolution or thermodynamics turbulent Navier-Stokes equations for air.
- Numerical resolution of the heat transfer equation trough the envelope.
- Upgrading of indoor air temperatures.

A flowchart of the numerical code is shown in Figure 9.

5.2 Numerical approximation of involved equations

To numerically solve the thermodynamic turbulent Navier-Stokes equations governing air dynamics, a mixed $\mathbb{P}2$–$\mathbb{P}1$ finite element approach was employed for velocity and pressure, while a $\mathbb{P}1$ approximation was utilized for temperature. The numerical discretization was performed by using the method of characteristics ir order to guarantees the positivity of the scheme (Hecht 2021) and prevent spurious oscillations (Gresho et al. 1980).

Equation (14) of heat conduction for the walls courtyard, the floor slab and roofs, was discretized in space by using a P1 Finite Element approximation while an implicit Euler finite difference scheme was used for time discretization. Finally, if no data of the indoor air temperatures are known, Equation (17) for every zone is approximated by using the called analytical approximation (EnergyPlus 2021; Domínguez-Torres et al. 2022).

5.3 Thermal boundary layers approach

In accordance with Section 4, the convective flux between external surfaces and air is computed using the expression

$$q_{c,S} = k_{air}\left(T_{air}(x_p) - T_S\right)$$

where $T_{air}(x_p)$ denotes the air temperature at the closest grid point x_p to the surface.

Achieving a precise estimation of heat transfer between surfaces and airflow necessitates the inclusion of grid nodes within the thermal turbulent boundary layer of the flow. To achieve this, it suffices for the distance dx_p from x_p to the surface to satisfy

$$dx_p < \delta \tag{18}$$

where δ is the thickness of thermal turbulent boundary layer (Schlichting and Gersten 2000). For the geometry considered and the mean velocity found, next to the surfaces a refined size mesh of 0.001 m was used in such a way that inequality (18) is verified (Zhai and Chen 2004).

6 Model validation

The validation process carried out is based, firstly, on the comparison between the monitored measurements and the simulated results, in order to draw conclusions on the qualitative behavior of the simulation output and, secondly, on the calculation of a set of statistical indices standardly applied for validation purposes of energy software for buildings. The most important features of the validation process performed are described next.

6.1 Experimental setup

The sensors used to collect wall surface temperatures and air temperatures inside the courtyard were placed as shown in Figure 10(a) and at two heights: 1.5 m and 4.5 m. The air

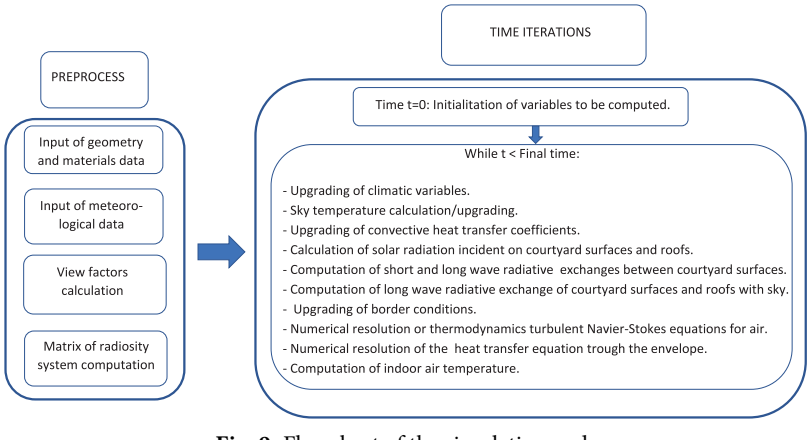

Fig. 9 Flowchart of the simulation code

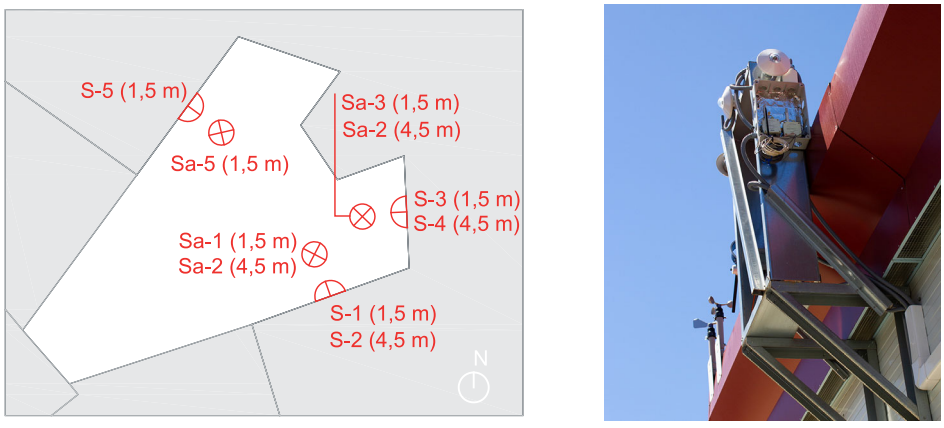

(a) (b)

Fig. 10 (a) Position of the monitoring sensors in the courtyard indicating height (S-1, S-2, S-3, S.4 and S-5: surface temperature sensors; Sa-1, Sa-2, Sa-3, Sa.4 and Sa-5: air temperature sensors); (b) weather station

sensors were placed in the same positions and at 0.2 m from the walls.

These sensors are of the type I2C digital with a typical accuracy of ±0.25 °C for a range from −40 °C to +125 °C and each of them was shielded against both long- and short-wave radiation.

The weather variables were measured from a weather station placed in a area belonging to the University of Sevilla at a distance of 300 m from the building used for the monitoring campaign, Figure 10(b). This weather station is equipped with: a set of five pyranometers with horizontal, north, east, south, and west orientation in order to have an accurate measurement of solar radiation; an anemometer and a vane for the wind speed and direction; a sensor for relative humidity of air, and finally two shielded sensors to register the dry bulb ambiance temperature. In Table 1 the characteristics of the weather sensors are shown. Measurements were recorded every five minutes.

Table 1 Specifications of the sensors installed in the weather station

Variable	Type of sensor	Accuracy	Rank
Global irradiance	Pyranometer	±1.5%	0 to 2000 W/m^2
Ambiance air dry bulb temperature	Thermometer	±0.75 °C	−40, 80 °C
Ambiance air relative humidity	Hygrometer	±3%	0 to 100 %
Wind speed	Anemometer	±0.5%	0 to 50 m/s
Wind direction	Vane	±2.5%	0 to 360°

6.2 Experimental and simulated results: qualitative comparison

The experimental measurements and numerical simulations were conducted over the period from July 1 to July 8, 2023. To take into account the effect of the thermal inertia of the wall and roof masses, the first three days of this period were used for warming purposes and only the results from July 4 to 8 were considered for validation purposes.

In Figure 11 the measured and simulated temperature profiles for the surface and air close to the southern wall of the courtyard (sensors S1, S2, Sa1 and Sa2) are shown. It can be observed that the computed results are quite close to the monitored results, and this supports the good qualitative performance of the numerical method for simulating the behavior of courtyard temperatures.

From the monitored results and the simulation results it can be deduced that the courtyard has a different temperature regime at daylight and at night. In daylight the temperatures inside the courtyard are lower than the outside temperature due to the effect of protection from solar radiation falling on the interior walls offered by the courtyard walls themselves, as well as the protection from the warm wind offered by these walls. This temperature behavior is also influenced by the thermal inertia of the masses of the walls themselves, which preserves the coolness of the night resulting from the radiative exchange with the sky and a certain conservation of a layer of cold night air that, due to its higher density, stagnates in the lower part of the courtyard, as shown in Figure 12. It can be seen that for days when the temperature is higher, the temperature difference between the air inside and the air outside the courtyard is greater, with the temperature in the lower part of the courtyard being 8 °C lower during the hours of maximum outdoor temperature.

On the contrary, during the night an opposite thermal behavior was found in which the ambient temperature is generally lower than inside the courtyard. This can have two relatively clear causes: on the one hand, due to the effect of accumulating heat in the walls of the courtyard which is released to the outside when the outdoor temperature drops

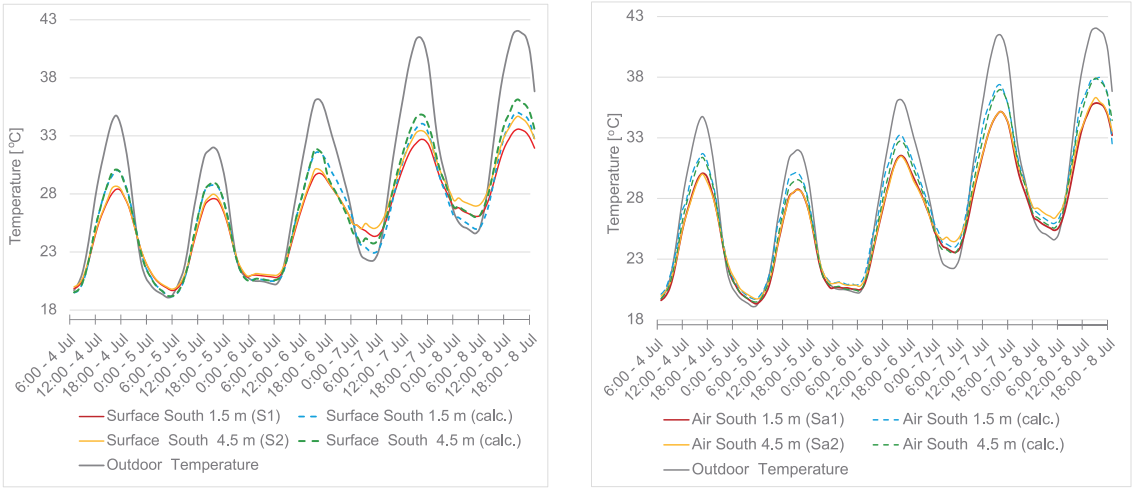

(a) (b)

Fig. 11 Simulated and measured temperatures on courtyard south face at 1.5 m and 4.5 m height: (a) for wall surface; (b) for air close to the wall

at night, and, on the other hand, the lower influence of radiative cooling due to the lower exposure of the courtyard surfaces to the sky, which makes them have a lower view factor with respect to the sky and therefore implies a reduction of the radiative exchange with the sky, usually at lower temperatures. This double behavior, diurnal and nocturnal, which is derived from the monitored data, is also replicated by the results from numerical simulation, which again highlights the model's ability to qualitatively predict the thermal behavior of the courtyard.

On the other hand, the simulations highlight the complex thermodynamics of the air in the courtyard under the effect of wind and natural convection. Thus, Figure 12 shows how the displacement of air from the roofs due to the effect of the wind produces an intrusion of outside air, partly heated by the action of the sun on the roofs, inside the courtyard. This air intrusion effect is reinforced by the upward flow of air in the warmer wall zones, which causes an air pressure drop in the interior zone of the courtyard, whose immediate effect is to enhance the entry of air from the zone opposite the warm wall, which results in an increase in the interior temperatures of the courtyard.

Moreover, a relatively rapid change in air temperature can be observed in Figure 12 for the time interval from 14 h to 14:20 h. As already mentioned, the thermodynamics of the air in the courtyard and adjacent roofs is complex, and so it is difficult to find a single cause for this effect, but it is most likely due to a combination of factors. On the one hand, the natural convection on the wall facing the sun, on the left in the figure, is intensified by the impact on this wall of the strong solar radiation typical of the central hours of a mid-summer day in southern Spain. This natural convection produces a depression inside the courtyard that causes an increase in the airflow entering from the upper zone after passing through the overheated bituminous roof, this airflow being also boosted by an increase in wind speed from 2.5 to 4 m/s, according to the measured values. In summary, the combined effect of air depression caused by natural convection together with wind-enhanced airflow, are likely the cause of the intrusion of warm air from the bituminous roof area, causing the relatively rapid temperature change for the day and time shown in the figure.

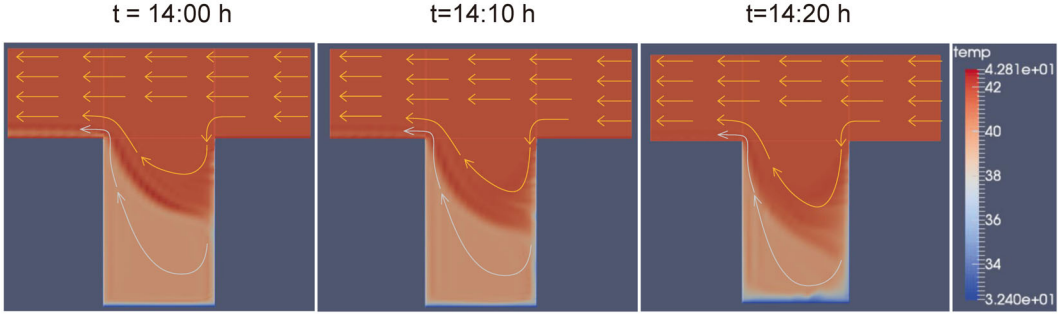

Fig. 12 Reference case: temperature pattern in a cross-section of the courtyard in the wind direction at 14:00, 14:10 and 14:20 h of 7 July 2023

6.3 Statistical validation

Multiple agencies have devised standards to assess the "level of reliability" of the true value when utilizing numerical simulation. Among these, the ASHRAE Guideline 14-2014, the International Performance Measurement and Verification Protocol (IPMVP), and the Federal Energy Management Program (FEMP) are widely acknowledged as prominent standards. The main indicators utilized by these agencies are (Ramos-Ruiz and Fernández-Bandera 2017): the normalized mean bias error (NMBE), the coefficient of variation of the root mean square error (CV(RMSE)) and coefficient of determination (r^2).

In addition to these indices, according to Willmott (1981) the root mean square error (RMSE) is also computed as well as the index of agreement d; d is a standardized index, with values between 0.0 and 1.0, indicating the accuracy of the simulated values relative to the measured values. A value d = 1.0 denotes exact correspondence between the measured and simulated temperature values. Appendix B gives the definition of d and Appendix C provides the values recommended by the aforamentioned agencies to consider validated a model.

The obtained values of the statistical indicators for the validation of the simulation model are presented in Table 2 for each sensor. From the values shown in this table, it can be concluded that the index of agreement d and the value of r^2 that are both greater than 0.90 for all cases, and the values of NMBE, CV(RMSE) and RMSE that are inside the range usually established by international agencies, Table A4, support the previous statement regarding the good accuracy of the developed simulation model.

Finally, it is noteworthy to observe that the values of RMSE are similar to the found in some previous works as Forouzandeh (2022) who reported an RMSE value of 0.92 °C for air close to walls inside a courtyard. Likewise, these values are clearly lower than those generated by the ENVI-met software (3.31 °C and 3.40 °C) and the Ladybug Tool (2.59 °C and 4.49 °C) for two summer periods similar to those examined in this research and for a courtyard in the same city of Seville (López-Cabeza et al. 2021).

Hence, the statistical validation indices derived for the numerical model developed are in accordance with the criteria forth by the referenced agencies and by Willmott (1981) to deem a model validated, thereby indicating that the developed simulation model is suitable for assessing the energy performance of courtyards.

Table 2 Validation statistical results

	Wall sensors				
Index	S1	S2	S3	S4	S5
NMBE [%]	1.19	1.31	−0.98	−1.01	1.44
CV(RMSE) [%]	3.444	3.648	3.8729	3.6434	4.8387
RMSE	0.907	0.948	0.991	1.028	1.182
r^2	0.9416	0.9698	0.9281	0.951	0.932
d	0.961	0.958	0.931	0.926	0.921
	Air sensors				
Index	Sa1	Sa2	Sa3	Sa4	Sa5
NMBE [%]	1.27	1.49	−1.66	−1.81	1.93
CV(RMSE) [%]	3.594	3.692	3.981	4.034	4.504
RMSE	1.237	1.1993	1.209	1.272	1.149
r^2	0.916	0.926	0.930	0.907	0.902
d	0.930	0.929	0.917	0.916	0.909

7 Impact of radiative cooling on the thermal and energy performance of the courtyard: comparative analysis

In this section, the effect on the thermal and energy performance of the courtyard case study described in Section 3 when subjected to the application of radiative cooling techniques is investigated using the simulation model introduced in Section 4.

7.1 Thermal performance analysis

The impact of the use of radiative cooling in the energy performance of buildings has been extensively analyzed in the literature, as evidenced in the reviews in Lu et al. (2016), Chen and Lu (2020) and Pirvaram et al. (2022), in addition to the references cited in the Introduction section. However, to our knowledge, no studies have been published about the impact on the thermal and energy performance of courtyards of the application of radiative cooling on courtyard walls and adjacent roofs.

For the analyzed case study, the courtyard walls with prevalent southern orientation are less affected by the shading from the courtyard, while other orientations capture a significant amount of solar radiation due to multiple reflections within the courtyard, storing it on the surfaces (Huang and Li 2017), which can counteract the decreased shortwave radiation on the surfaces as a consequence of the shading produced by the different walls of the courtyard, a fact that suggests the convenience of cooling these surfaces in order to reduce the global heat gain of the courtyard.

As is well known, the critical requirements for achieving cooling on surfaces exposed to the environment involve: (a) maximizing reflection across the solar spectrum (0.32–2.5 μm) to minimize sunlight absorption and (b) enhancing thermal emission within the infrared atmospheric transmission window (8–13 μm) to facilitate efficient outward thermal radiation (Zhang et al. 2022).

One of the most widely used radiative cooling techniques, due to its ease of implementation and lower economic cost in comparison to other more complex techniques, is the application of paints with high reflectivity to solar radiation and highly reflective on the infrared atmospheric transmission window (Das et al. 2023).

In this research, the ultra-emissive paint developed by Das et al. (2023) that exhibits a solar reflectance of 96.3% and a thermal emissivity of 98.5% at the atmospheric transmission window was used as the radiative cooling technique implemented. This paint is considered to be applied to all wall surfaces facing the courtyard and also on adjacent roofs.

Considering the aforementioned fact that the wind moves air over the roofs and some of it enters the courtyard, as was shown in Section 6.2, the fact that the roofs are cool and reach much lower temperatures than when covered with bituminous paint is a feature that can be exploited to improve the cooling of the courtyard.

In addition, the intromission of air from the roofs into the courtyard is enhanced due to the cooling of the air when in contact with the cool roofs and the dragging of this cooled air by the effect of the wind toward the air zone of the courtyard, so that the higher density of this cold air causes it to enter the interior of the courtyard. As a result of this process, an increase in the temperature difference of the air inside the courtyard with respect to the warm air outside is expected, which is obviously desirable in the warm season.

This cooling effect is enhanced by the use of the radiative cool paint on the courtyard walls, reducing the heat accumulation on the walls, which has the double effect of reducing the courtyard temperatures during the day while positively affecting the night temperature due to less heat accumulation during the day, which ultimately implies a reduction of heat flux into the building and better comfort conditions during the day and night.

To analyze the effect of the application of the referred paint on the energy performance of the courtyard, the previously numerical model introduced is applied to the case study under the assumption of the application of the ultra-emissive paint developed by Das et al. (2023) on the walls of the courtyard and adjacent roofs.

As a first result of these simulations, in Figure 13 the temperature pattern of the airflow is illustrated. As can be seen in the figure, the displacement of the air forced by the wind causes air to enter the courtyard similar to the reference case, with the difference that now this air comes partly from the cooler surface of the roof covered by the reflective cool paint. In this way, the air inside the courtyard remains at a cooler temperature than in the reference case, maintaining a cool air zone caused by the lower temperature of the courtyard walls due to the cold paint applied and the cold air coming from the cool roof. Next, the values of the temperature of the air inside the courtyard and adjacent walls for the radiative cooled case are compared with the temperatures obtained for the reference case.

In Figure 14(a) the hourly temperatures of the reference case and the cool case are reported for the time interval from 4 to 8 July of 2023 and for the courtyard south wall at 1.5 m and 4.5 m height (sensors position S1 and S2). As can be seen in this figure, the temperatures for the radiative-cooled courtyard are, without exception, lower than those provided by the reference case, with a decrease with respect to the reference case, which, as shown in Figure 14(b), is above 4 °C for the hours of highest outdoor temperature values.

Regarding the outdoor temperature, the cool case is able to provide reductions up to 12 °C in the hours when the outdoor temperature reaches its highest value, while the reduction provided by the reference case is about 8 °C for the same hours.

At night, the cool courtyard reduces the overheating observed in the reference case. Thus, at night, although the temperatures in the cool case are not always lower than the outside temperatures, they do represent a significant reduction with respect to the reference case, which has an obvious impact on the comfort of the spaces adjacent to the courtyard and inside the courtyard itself, especially when the outside temperatures approach 25 °C at night, temperatures that can be considered as incompatible

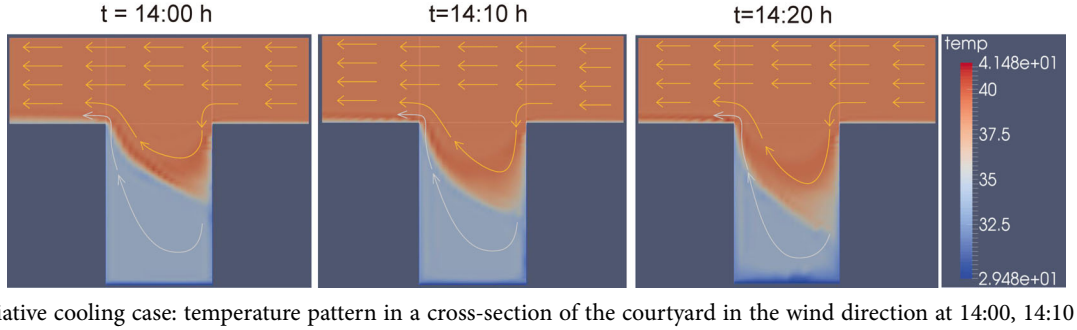

Fig. 13 Radiative cooling case: temperature pattern in a cross-section of the courtyard in the wind direction at 14:00, 14:10 and 14:20 h of 7 July 2023

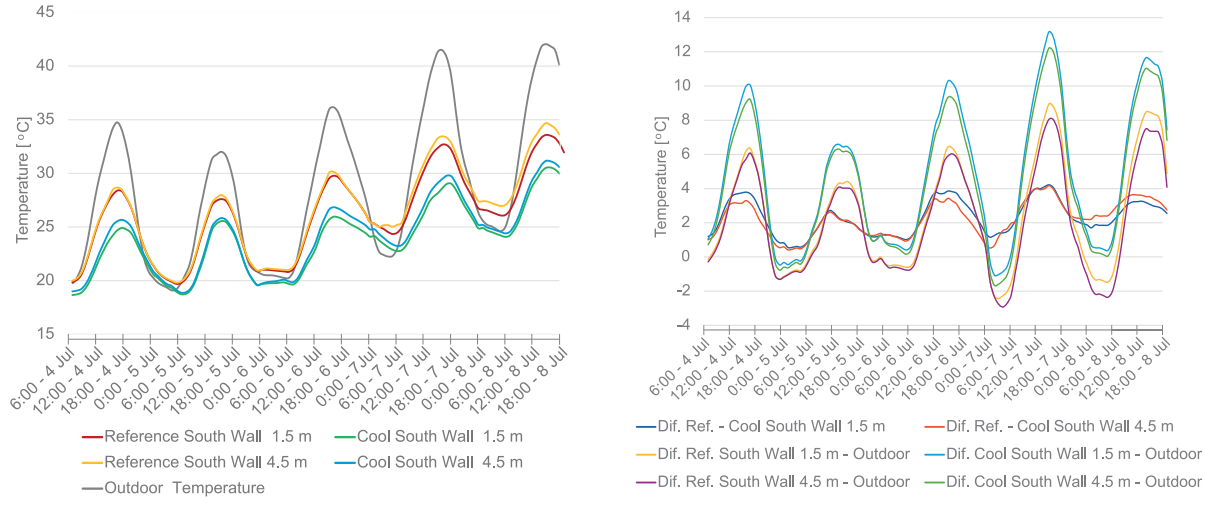

(a) (b)

Fig. 14 (a) South wall temperatures at 1.5 m and 4.5 m for the reference and the cool cases; (b) south wall temperatures difference at 1.5 m and 4.5 m

with a quality night's rest and that for the reference case is aggravated by overheating that can reach 3 °C as observed in Figure 14(b).

Similar behavior can be observed for air temperatures in sensor positions Sa1 and Sa2, as can be seen in Figure 15.

In Table 3 the minimum and maximum daily temperatures measured at the sensors locations for the reference and cool courtyard are shown. As can be seen, for the reference case the minimum temperatures are practically always higher than the outdoor temperatures, in accordance with the nocturnal overheating noted above, while the maximum daily temperature is always lower, although the reduction is less than for the cool case. In this case it is also observed that the minimum temperatures are in some nights lower than the outdoor temperatures, although on other days they are higher than the outdoor temperatures, which implies a certain overheating effect, although much lower than in the reference case.

7.2 Energy analysis

The energy analysis is focused in the assessment of the thermal loads, and associated savings, for the adjacent indoor spaces of the courtyard. For reasons of space only the results for the first and second floors of the south-east and north-west courtyard walls are presented.

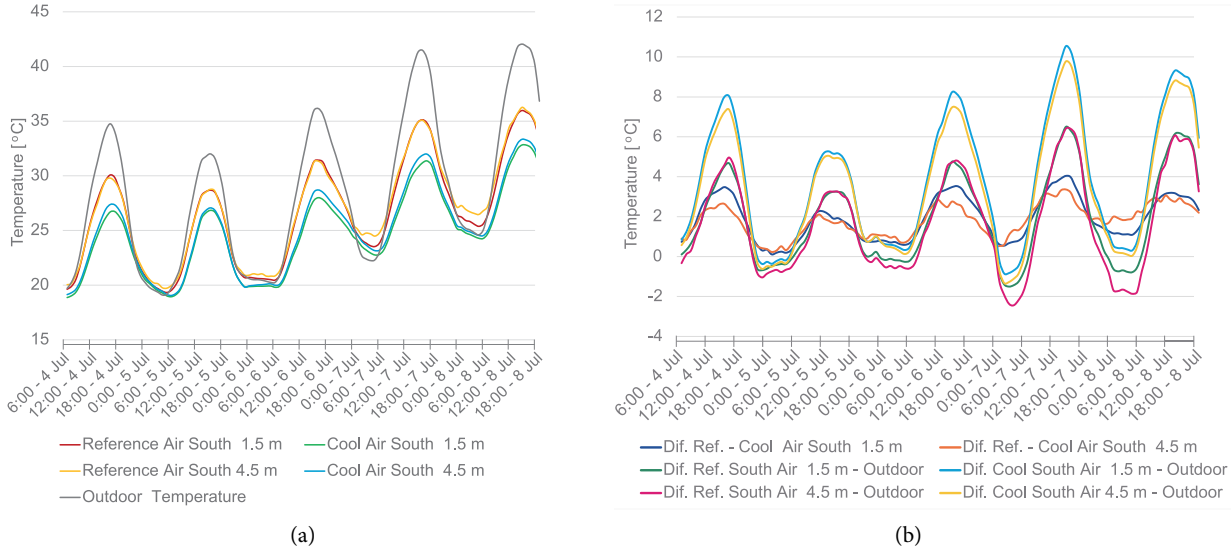

(a) (b)

Fig. 15 (a) Air temperatures at 1.5 m and 4.5 m close to southern wall for the reference and the cool cases; (b) difference air temperatures at 1.5 m and 4.5 m

Table 3 Reference and cool cases: minimum and maximum daily temperature

	Reference case									
	4 July		5 July		6 July		7 July		8 July	
Position	Min	Max	Min	Max	Min	Max	Min	Max	Min	Max
Outdoor	19.25	34.75	19.09	32.01	20.50	36.15	22.30	41.48	24.60	42.05
S1	19.81	28.39	19.69	27.59	20.81	29.77	24.35	32.67	26.07	33.58
Sa1	19.48	30.08	19.32	28.68	20.46	31.43	23.60	35.12	25.37	35.97
S2	19.94	28.66	19.80	27.98	21.00	30.11	25.01	33.44	27.06	34.68
Sa2	19.78	29.79	19.72	28.75	20.82	31.34	24.48	35.08	26.46	36.26
S3	19.75	28.32	19.65	27.54	20.79	29.86	24.32	32.76	26.09	33.56
Sa3	19.45	28.89	19.32	28.70	20.43	31.36	23.60	35.07	25.48	35.60
S4	19.94	28.67	19.80	27.98	21.00	30.11	25.01	33.45	26.96	34.68
Sa4	19.86	29.77	19.61	28.77	20.97	31.50	24.70	35.28	26.49	35.87
S5	20.10	28.98	19.88	27.74	21.14	30.47	24.07	34.89	25.91	36.78
Sa5	19.98	29.86	19.74	28.58	21.04	31.73	23.65	36.04	25.55	38.00
	Cool case									
	4 July		5 July		6 July		7 July		8 July	
Position	Min	Max	Min	Max	Min	Max	Min	Max	Min	Max
Outdoor	19.25	34.75	19.09	32.01	20.50	36.15	22.30	41.48	24.60	42.05
S1	18.65	24.90	18.74	25.54	19.64	25.96	22.75	29.03	24.07	30.54
Sa1	18.85	26.72	18.93	26.83	19.80	28.00	22.76	31.36	24.26	32.82
S2	18.99	25.66	18.88	25.82	19.86	26.84	23.23	29.73	24.40	31.16
Sa2	19.12	27.38	19.05	27.06	19.99	28.70	23.16	31.98	24.52	33.34
S3	18.88	25.01	19.01	25.66	19.73	25.90	22.84	29.17	24.21	30.86
Sa3	18.55	25.33	18.93	25.80	19.01	26.12	22.72	30.39	23.90	31.49
S4	19.13	25.06	18.77	25.63	20.11	25.59	22.97	29.02	24.33	30.66
Sa4	18.91	26.11	18.33	25.98	19.79	26.21	22.51	30.11	24.00	31.26
S5	19.30	25.88	19.66	26.11	20.12	26.79	23.11	29.88	24.41	32.51
Sa5	19.11	26.31	19.10	26.05	20.07	26.88	23.82	30.31	24.82	33.78

To do this analysis, first the heat fluxes through the courtyard walls for the reference case, Q_{Ref}, and for the radiative cooling case, Q_{RadCool}, are computed. According to the procedure from Gagliano et al. (2016), to calculate Q_{Ref} and Q_{RadCool} the following expressions are used:

$$Q_{\text{Ref}} = \frac{1}{R_{\text{W}}} \sum_{t=t_{\text{ini}}}^{t_{\text{end}}} \left(TS_{\text{Ref}}(t) - T_{\text{ind}}(t) \right) \quad [\text{W/m}^2]$$
$$Q_{\text{RadCool}} = \frac{1}{R_{\text{W}}} \sum_{t=t_{\text{ini}}}^{t_{\text{end}}} \left(TS_{\text{RadCool}}(t) - T_{\text{ind}}(t) \right) \quad [\text{W/m}^2] \tag{19}$$

where $TS_{\text{Ref}}(t)$ and $TS_{\text{RadCool}}(t)$ are respectively the temperatures at the exterior surface of the wall for the reference case and the radiative cooled case at time t, $T_{\text{ind}}(t)$ is the indoor temperature, and R_{W} is the thermal resistance of the wall W. Equation (19) implies that the heat flux is considered positive if it enters the indoor space and negative if it flows to the outside.

The wall thermal resistance R_{W} used in the computations of Q_{Ref} and Q_{RadCool} in Equation (19), is defined as:

$$R_{\text{W}} = \frac{1}{h_{\text{c,r}}} + \sum_{j=1}^{5} \left(\frac{e_j}{\lambda_j} \right) \quad [\text{m}^2 \cdot \text{W/K}] \tag{20}$$

where e_j and λ_j are, respectively, the thickness and thermal conductivity of the j-th layer of the wall as described in Table A1, and $h_{\text{c,r}}$ is the mixed convective-radiative heat transfer coefficient between the interior surface of the wall and the indoor ambient that, following ASHRAE criteria, is taken as $h_{\text{c,r}} = 8.29$ [W/(m²·K)], as stated in Section 4.7.

For the interior spaces a continuous mode of the conditioning system was assumed. The indoor temperature was set at 25 °C according to that established as the comfort temperature for the cooling season by the Spanish building energy regulations (RITE 2021). Then, the thermal loads were computed for the time interval of study and for the

zones corresponding to the first floor (0–3 m height) and to the second floor (3–6 m height), at the vertical of positions S-1 and S-5 marked in Figure 10(a). The values of the calculated thermal loads, as well as the associated savings, are shown in Table 4.

From the results shown in Table 4, it can be concluded that the radiative cooling technique applied to the courtyard can provide significant reductions in thermal loads.

Thus, for the spaces analyzed, the thermal load savings ranged from a minimum of 184.35 [Wh/m^2] to a maximum of 189.0 [Wh/m^2], equivalent to a reduction of 63.46 % and 69.85%, respectively.

The southeast wall of the courtyard provides slightly better performance than the northwest wall, and in addition, the lower floors provide greater reduction on each facade than the higher floors. Thus, for the southeast, the first floor provides a reduction of 189.08 [Wh/m^2] versus a reduction of 187.96 [Wh/m^2] for the second floor, equivalent to a reduction in thermal loads of 69.85% and 66.88 % respectively. For the northwest wall of the courtyard , the first floor produces a reduction of 184.59 [Wh/m^2], while the second floor provides a reduction of 184.35 [Wh/m^2], equivalent to a reduction of 63.93% and 63.46 %, respectively. Although in this case the thermal loads are very close, the same pattern of a larger reduction of thermal loads is also observed as the floor is lower.

The cause of the observed differences in thermal loads may be due to many factors, such as differences in air temperature in contact with the walls, which are not uniform as seen above, or differences in solar radiation exposure and radiative exchange with the sky, which may be different for each orientation and wall height. Therefore, a more in-depth study on the inhomogeneity of the effect of radiative cooling in the different areas of the courtyard could be clarifying, a study that is beyond the scope of the present work but could be the subject of future research.

8 Conclusions

This study investigates the impact on the thermal and energy performance of a courtyard of the application of radiative cooling and compares it to that of a conventional courtyard. The radiative cooling technique implemented consists of the application of an ultra-emissive and highly sun-reflective paint to the courtyard surfaces and adjacent roofs.

A numerical model is developed to perform the energy analysis. The model applies a mixed ray tracing-radiosity method to calculate the impact and reflections of solar radiation on the courtyard surfaces, as well as the long-wave radiative exchanges in these surfaces. The numerical model also uses a turbulent κ-ε model with a Bousinesq approximation for natural convection to simulate the thermodynamic airflow on the roofs and inside the courtyard. This model was validated by means of an empirical validation procedure that demonstrated its ability to estimate with a high degree of accuracy the behavior of temperatures on the surfaces and air of the courtyard.

In view of the results obtained from the analyzed case study, it can be concluded that the application of the highly ultra-emissive paint considered on the courtyard enhances its ability to achieve temperatures lower than those in the surrounding environment. This way, without any exception in the period of time analyzed, the courtyard cool exhibits lower temperatures than those of the reference case. Thus, for the time period analyzed, the reference courtyard temperatures range from a minimum of 19.32 °C to a maximum of 38.00 °C, while for the cold courtyard the temperatures range from a minimum of 18.33 °C to a maximum of 33.78 °C. With respect to the base case, the cool courtyard shows a drop in temperatures than can reach 4 °C, while with respect to the outdoor air, in the hours of higher temperatures it is able to produce a drop in temperatures of about 12 °C .

The ability of the cool courtyard to mitigate the overheating effect observed during the night hours was also observed, being able to eliminate this effect in half of the nights studied and significantly reduce it in the rest of the nights.

In regards to the thermal loads to achieve indoor comfort in the spaces adjacent to the courtyard, it was found that the cool courtyard can substantially reduce them and provide significant savings compared to the reference case. Thus, for the time period analyzed, the reductions in thermal load ranged from a minimum of 184.35 [Wh/m^2] to a maximum of 189.0 [Wh/m^2], equivalent to a decrease of

Table 4 Thermal loads for courtyard adjacent spaces

	South-east (first floor)	South-east (second floor)	North-west (first floor)	North-west (second floor)
Reference base loads [Wh/m^2]	270.67	281.04	288.72	290.45
Rad. cool base loads [Wh/m^2]	81.58	93.63	104.13	106.11
Savings [Wh/m^2]	189.08	187.96	184.59	184.35
Savings [%]	69.85	66.88	63.93	63.46

63.46% and 69.85%, respectively, with the greatest savings obtained on the lower floors and on the southeast wall of the courtyard.

In summary, it can be concluded that the analyzed radiative cooling technique is able to improve the cooling effect of the courtyard in the warm season and can be considered a very useful tool to cope with overheating in warm and sunny geographical areas.

Appendix

Appendix A. Envelope description

In this appendix the thermophysical properties of the courtyard walls, floor slab and adjacent roofs are described. The data shown in Tables A1, A2 and A3 correspond to the nominal values and were based on the Spanish Building Code (CTE 2020) and specifications from manufacturers.

Table A1 Thermophysical properties of the building walls

Layer	Description	Thickness [m]	Density [kg/m^3]	Specific heat [J/(kg·K)]	Conductivity [W/(m·K)]
1 (Out.)	Cement rendering	0.015	1300	1000	0.67
2	Perforated brick	0.115	780	1000	0.35
3	Cement rendering	0.010	1300	1000	0.67
4	Air chamber	0.05	1.184	1007	0.02551
5	Hollow brick	0.04	770	1000	0.32
6 (In.)	Gypsum plaster	0.015	1000	1000	0.57

Table A2 Thermophysical characteristics of the reference roof

Layer	Description	Thickness [m]	Density [kg/m^3]	Specific heat [J/(kg·K)]	Conductivity [W/(m·K)]
1 (Ext.)	Bituminous paint	0.0015	1150	1000	0.23
2	Ceramic tiles	0.005	2000	800	1.00
3	Mortar	0.01	2000	1000	1.40
4	Protective Layer	0.015	1150	1000	0.23
5	Mortar	0.01	2000	1000	1.40
6	Carbon cinders	0.1	640	657	1.40
7	Concrete vault	0.22	1330	1000	1.32
8 (Int.)	Gypsum plaster	0.01	1000	1000	0.32

Table A3 Thermophysical characteristics of the floor slab

Layer	Description	Thickness [m]	Density [kg/m^3]	Specific heat [J/(kg·K)]	Conductivity [W/(m·K)]
1 (Ext.)	Ceramic tiles	0.005	2000	800	1.00
2 (Int.)	Concrete	0.20	2000	1000	1.35

Appendix B. Index of agreement determination

In this appendix the calculation of the index of agreement d (Willmott 1981) is described. For this, if $T_m(t)$ and $T_s(t)$ are respectively the measured and simulated temperatures at time $t \in [t_1, t_N]$, the following variables are computed:

- The means $\overline{T}_m$, $\overline{T}_s$.
- $\tilde{T}_s(t) = T_s(t) - \overline{T}_m$ and $\tilde{T}_m(t) = T_m(t) - \overline{T}_m$.
- Then, the index of agreement d is obtained from

$$d = 1 - \frac{\sum_{t=t_1}^{t_N} \left(T_s(t) - T_m(t)\right)^2}{\sum_{t=t_1}^{t_N} \left(|\tilde{T}_s(t)| + |\tilde{T}_m(t)|\right)^2} \quad \text{(A1)}$$

Appendix C. Agencies validation criteria

Here the model validation criteria of ASHRAE Guideline-12, FEMP and IPMVP to consider validated a energy model are shown for hourly data.

Table A4 Model validation criteria for hourly data

Index	ASHRAE Guidelines	FEMP	IPMVP
NMBE [%]	$\in [-10,10]$	$\in [-10,10]$	$\in [-5,5]$
CV(RMSE) [%]	<30	<30	<20
r^2	>0.75	>0.75	—

Acknowledgements

This research was funded by the Ministry of Economy and Competitiveness of the Spanish Government and the European Regional Development Fund through the research and development project "Parametric Optimization of Double Skin Facades in the Mediterranean Climate to Improve Energy Efficiency Under Climate Change Scenarios" (ref BIA2017-86383-R).

Funding note: Funding for open access publishing: Universidad de Sevilla/CBUA.

Declaration of competing interest

The authors have no competing interests to declare that are relevant to the content of this article.

Author contribution statement

All authors have contributed: in the study conception and design, in the analysis and interpretation of the data; in

drafting and revising the article and in the approval of the final manuscript version.

References

AEMET (2010) Guía resumida del clima en españa (1981–2010). Tech. rep., Agencia Estatal de Meteorología de España, Spain. Available at https://www.aemet.es/es/. (in Spanish)

Al-Hafith O, Satish BK, Bradbury S, et al. (2017). Simulation of courtyard spaces in a desert climate. *Energy Procedia*, 142: 1997–2002.

Amraoui K, Sriti L, Di Turi S, et al. (2021). Exploring building's envelope thermal behavior of the neo-vernacular residential architecture in a hot and dry climate region of Algeria. *Building Simulation*, 14: 1567–1584.

Antoniou N, Montazeri H, Neophytou M, et al. (2019). CFD simulation of urban microclimate: Validation using high-resolution field measurements. *The Science of the Total Environment*, 695: 133743.

ASHRAE (1997). ASHRAE Fundamentals Handbook (SI). Atlanta, GA, USA: American Society of Heating, Refrigerating and Air Conditioning Engineers.

Bahadori MN (2011). Passive cooling techniques in Iranian architecture. In: Renewable Energy. London: Routledge.

Bejan A (1992). Heat Transfer. New York: John Wiley & Sons.

Blocken B (2015). Computational fluid dynamics for urban physics: Importance, scales, possibilities, limitations and ten tips and tricks towards accurate and reliable simulations. *Building and Environment*, 91: 219–245.

Cattarin G, Pagliano L, Causone F, et al. (2018). Empirical and comparative validation of an original model to simulate the thermal behaviour of outdoor test cells. *Energy and Buildings*, 158: 1711–1723.

Cengel Y (1992). Heat Transfer. New York: McGrawHill.

Chandel SS, Sharma V, Marwah BM (2016). Review of energy efficient features in vernacular architecture for improving indoor thermal comfort conditions. *Renewable and Sustainable Energy Reviews*, 65: 459–477.

Chen J, Lu L (2020). Development of radiative cooling and its integration with buildings: A comprehensive review. *Solar Energy*, 212: 125–151.

Chen L, Zhang K, Ma M, et al. (2020). Sub-ambient radiative cooling and its application in buildings. *Building Simulation*, 13: 1165–1189.

Clark G, Allen C (1978). The estimation of atmospheric radiation for clear and cloudy skies. In: Proceedings of the 2nd National Passive Solar Conference (AS/ISES).

Coussirat M, Guardo A, Jou E, et al. (2008). Performance and influence of numerical sub-models on the CFD simulation of free and forced convection in double-glazed ventilated façades. *Energy and Buildings*, 40: 1781–1789.

CTE (2020). Prontuario de soluciones constructivas del CTE. Instituto de Ciencias de la Construcción Eduardo Torroja. Available at http://cte-web.iccl.es/materiales.php. (in Spanish)

Das P, Rudra S, Maurya KC, et al. (2023). Ultra-emissive MgO-PVDF polymer nanocomposite paint for passive daytime radiative cooling. *Advanced Materials Technologies*, 8: 2301174.

Domínguez-Delgado A, Domínguez-Torres H, Domínguez-Torres CA (2020). Energy and economic life cycle assessment of cool roofs applied to the refurbishment of social housing in southern Spain. *Sustainability*, 12: 5602.

Domínguez-Torres CA, León-Rodríguez AL, Suárez R, et al. (2019). Numerical and experimental validation of the solar radiation transfer for an egg-crate shading device under Mediterranean climate conditions. *Solar Energy*, 183: 755–767.

Domínguez-Torres CA, Suárez R, León-Rodríguez AL, et al. (2022). Experimental validation of a dynamic numeric model to simulate the thermal behavior of a facade. *Applied Thermal Engineering*, 204: 117686.

EnergyPlus (2021). EnergyPlus—Engineering Reference. Available at https://energyplus.net

European Commission (2014). Directorate-General for Energy. Technical Report, European Commission. Available at https://ec.europa.eu/clima/policies/strategies/2030-en

European Commission (2015). Financing the energy renovation of buildings with cohesion policy funding. Technical Report, European Commission.

Fernández Díaz P (2010). Centrales térmicas. biblioteca sobre ingeniería energética. Universidad de Cantabria. Available at https://pfernandezdiez.es/es/libro?id=15.

Fernandez N, Wang W, Alvine K, et al. (2015). Energy savings potential of radiative cooling technologies. Office of Scientific and Technical Information (OSTI).

Forouzandeh A (2018). Numerical modeling validation for the microclimate thermal condition of semi-closed courtyard spaces between buildings. *Sustainable Cities and Society*, 36: 327–345.

Forouzandeh A (2022). Comparative analysis of sol-air temperature in typical open and semi-closed courtyard spaces. *Building Simulation*, 15: 957–973.

Gagliano A, Nocera F, Aneli S (2016). Thermodynamic analysis of ventilated façades under different wind conditions in summer period. *Energy and Buildings*, 122: 131–139.

Goldstein EA, Raman AP, Fan S (2017). Sub-ambient non-evaporative fluid cooling with the sky. *Nature Energy*, 2: 17143.

Granqvist CG, Niklasson GA (2018). Solar energy materials for thermal applications: A primer. *Solar Energy Materials and Solar Cells*, 180: 213–226.

Gresho PM, Lee RL, Chan ST, et al. (1980). Solution of the time-dependent incompressible Navier-Stokes and Boussinesq equations using the Galerkin finite element method. In: Rautmann R (Ed), Approximation Methods for Navier-Stokes Problems. Berlin: Springer.

Hay H, Yellott J (1969). Natural air conditioning with roof ponds and movable insulation. *ASHRAE Transactions*, 75(1): 165–177

Hecht F (2012). New development in freefem++. *Journal of Numerical Mathematics*, 20(3–4): 251–265.

Hecht F (2021). FreeFEM Documentation. Release 4.6. Available at https://freefem.org/

Huang KT, Li YJ (2017). Impact of street canyon typology on building's peak cooling energy demand: A parametric analysis using orthogonal experiment. *Energy and Buildings*, 154: 448–464.

INDEX (2024). INDEX Construction System and Products. White reflex. Available at https://www.index-spa.com

IPCC (2014). Climate Change 2014, Synthesis Report. The Intergovernmental Panel on Climate Change. Available at https://www.ipcc.ch/site/assets/uploads/2018/05/SYR_AR5_FINAL_full_wcover.pdf

Isaac M, van Vuuren DP (2009). Modeling global residential sector energy demand for heating and air conditioning in the context of climate change. *Energy Policy*, 37: 507–521.

Judkoff R, Wortman D, O'Doherty B, et al. (2008). A methodology for validating building energy analysis simulations. National Renewable Energy Laboratory Golden, CO, USA.

Kuhn TE, Bühler C, Platzer WJ (2001). Evaluation of overheating protection with Sun-shading systems. *Solar Energy*, 69: 59–74.

López-Cabeza VP, Galán-Marín C, Rivera-Gómez C, et al. (2018). Courtyard microclimate ENVI-met outputs deviation from the experimental data. *Building and Environment*, 144: 129–141.

López-Cabeza VP, Carmona-Molero FJ, Rubino S, et al. (2021). Modelling of surface and inner wall temperatures in the analysis of courtyard thermal performances in Mediterranean climates. *Journal of Building Performance Simulation*, 14: 181–202.

Lu X, Xu P, Wang H, et al. (2016). Cooling potential and applications prospects of passive radiative cooling in buildings: the current state-of-the-art. *Renewable and Sustainable Energy Reviews*, 65: 1079–1097.

Mills A (1998). Heat Transfer, 2nd edn. Upper Saddle River, NJ, USA: Prentice Hall.

NBE-CT-79 (1979). Royal decrete 2429/1979: Approving the basic building on thermal conditions in buildings nbe-ct-79. Tech. rep., Spanish-Government, bOE Nro. 253; 6 July. pp. 24524-24550.

Pirvaram A, Talebzadeh N, Leung SN, et al. (2022). Radiative cooling for buildings: A review of techno-enviro-economics and life-cycle assessment methods. *Renewable and Sustainable Energy Reviews*, 162: 112415.

Raman A, Anoma M, Zhu L, et al. (2014). Passive radiative cooling below ambient air temperature under direct sunlight. *Nature*, 515(7528): 540–544.

Ramos-Ruiz G, Fernández-Bandera C (2017). Validation of calibrated energy models: Common errors. *Energies*, 10: 1587.

Rephaeli E, Raman A, Fan S (2013). Ultrabroadband photonic structures to achieve high-performance daytime radiative cooling. *Nano Letters*, 13: 1457–1461.

RITE (2021). Reglamento de instalaciones térmicas en los edificios. Tech. rep., Ministerio para la Transición Ecológica y el Reto Demográfico. Spanish Government. Available at https://energia.gob.es/desarrollo/EficienciaEnergetica/RITE/Paginas/InstalacionesTermicas.aspx. (in Spanish)

Sadeghipour Roudsari M, Pak M (2013). Ladybug: A parametric environmental plugin for Grasshopper to help designers create an environmentally-conscious. In: Proceedings of the 13th International IBPSA Building Simulation Conference Chambéry, France.

Sanjuan C, Suárez MJ, Blanco E, et al. (2011). Development and experimental validation of a simulation model for open joint ventilated façades. *Energy and Buildings*, 43: 3446–3456.

Santamouris M (2016). Cooling the buildings: Past, present and future. *Energy and Buildings*, 128: 617–638.

Santamouris M, Kolokotsa D (2015). On the impact of urban overheating and extreme climatic conditions on housing, energy, comfort and environmental quality of vulnerable population in Europe. *Energy and Buildings*, 98: 125–133.

Santamouris M, Yun GY (2020). Recent development and research priorities on cool and super cool materials to mitigate urban heat island. *Renewable Energy*, 161: 792–807.

Schlichting H, Gersten K (2000). Boundary-Layer Theory, 8th edn. Berlin: Springer.

SNSI (2021). Tech.report. Spanish National Statistics Institute. Government of Spain. Madrid, Spain. Available at https://www.ine.es/censos2021/

Sproul AB (2007). Derivation of the solar geometric relationships using vector analysis. *Renewable Energy*, 32: 1187–1205.

Taleghani M, Tenpierik M, van den Dobbelsteen A (2014). Indoor thermal comfort in urban courtyard block dwellings in the Netherlands. *Building and Environment*, 82: 566–579.

Tsoka S, Tsikaloudaki A, Theodosiou T (2018). Analyzing the ENVI-met microclimate model's performance and assessing cool materials and urban vegetation applications—A review. *Sustainable Cities and Society*, 43: 55–76.

Vautard R, Gobiet A, Sobolowski S, et al. (2014). The European climate under a 2 °C global warming. *Environmental Research Letters*, 9: 034006.

Walton G (1983). Thermal analysis research program reference manual. National Bureau of Standards NBSSIR 83-2655.

Willmott CJ (1981). On the validation of models. *Physical Geography*, 2: 184–194.

Zamani Z, Heidari S, Hanachi P (2018). Reviewing the thermal and microclimatic function of courtyards. *Renewable and Sustainable Energy Reviews*, 93: 580–595.

Zhai Z, Chen Q (2004). Numerical determination and treatment of convective heat transfer coefficient in the coupled building energy and CFD simulation. *Building and Environment*, 39: 1001–1009.

Zhai Y, Ma Y, David SN, et al. (2017). Scalable-manufactured randomized glass-polymer hybrid metamaterial for daytime radiative cooling. *Science*, 355: 1062–1066.

Zhang Q, Wang S, Wang X, et al. (2022). Recent progress in daytime radiative cooling: Advanced material designs and applications. *Small Methods*, 6(4): 2101379.